THESIS FOR THE DEGREE OF LICENTIATE OF ENGINEERING

Towards measuring quantum sound

Maria K. Ekström

Quantum Device Physics
Department of Microtechnology and Nanoscience (MC2)
Chalmers University of Technology
Göteborg, Sweden 2016

Towards measuring quantum sound

Maria K. Ekström, Göteborg, November 2016

© MARIA K. EKSTRÖM, 2016

Quantum Device Physics
Department of Microtechnology and Nanoscience (MC2)
Chalmers University of Technology
SE-412 96 Göteborg, Sweden
Telephone: +46 (0)31-772 1000

ISSN 1652-0769
Technical Report MC2-351

Front cover: Artistic illustration of an artificial atom emitting sound waves (not to scale). From the right, an artificial atom generates sound waves consisting of ripples on the surface of the substrate. The sound, known as a surface acoustic waves (SAWs) are picked up by a ”microphone” composed of interdigital transducer situated to the left. According to theory, the sound consists of individual quantum particles, the weakest whisper physically possible. Credit: Philip Krantz, Krantz NanoArt

Printed by Chalmers Reproservice
Göteborg, Sweden 2016

Towards measuring quantum sound

MARIA K. EKSTRÖM

Quantum Device Physics
Department of Microtechnology and Nanoscience (MC2)
Chalmers University of Technology

Abstract

One of the most fundamental phenomena occurring in nature is the interaction between single atoms and electromagnetic fields. This is studied in quantum optics to probe the quantum nature of the system. In appended Paper I, we demonstrated that an artificial atom can couple to propagating sound, which is the acoustic analogue of quantum optics. This thesis covers experiments where surface acoustic waves (SAWs) are used in superconducting circuits at gigahertz frequencies with the aim for quantum applications.

Since SAWs are mechanical vibrations that propagate on the surface of solids and dissipate little power, they can propagate freely over long distances before and after they interact with the artificial atom. Their five order of magnitude slower speed and smaller wavelength than light at gigahertz frequencies, open up for exploring new regimes of quantum physics. In addition, the coupling between the artificial atom and the SAWs is promising for reaching ultrastrong coupling limits, which is hard in other types of systems. Many of the future applications are discussed in appended Paper II, together with a more detailed description of the theory and fabrication of the devices.

Although the possibilities are many, a variety of potential experiments would benefit from higher conversion efficiency between electric signals and SAWs. Therefore, improvements of this conversion are studied in appended Paper III, making use of the many advances in classical SAW devices. More specifically, the conversion of unidirectional transducers (UDTs) on lithium niobate is studied and compared to symmetric interdigital transducers (IDTs). The results show that 99.4 % of the acoustic power can be focused in the desired direction and that the conversion between electric signals and SAWs is greatly improved by using UDTs, eliminating the largest contribution to loss of the IDTs. However, there is a trade-off between conversion efficiency and bandwidth. This knowledge allows us to better tailor potential quantum experiments based on SAWs, possibly towards measuring quantum sound.

Keywords: surface acoustic wave, interdigital transducer, unidirectional transducer, quantum acoustics, superconducting circuits, artificial atom, qubit, phonon, gigahertz frequency, cryogenic temperature,

List of appended papers

This thesis is based on the work contained in the following papers:

I **Propagating phonons coupled to an artificial atom**
Martin V. Gustafsson, Thomas Aref, Anton Frisk Kockum, **Maria K. Ekström**, Göran Johansson and Per Delsing
Science **346**, 207 (2014)

II **Quantum Acoustics with Surface Acoustic Waves**
Thomas Aref, Per Delsing, **Maria K. Ekström**, Anton Frisk Kockum, Martin V. Gustafsson, Göran Johansson, Peter Leek, Einar Magnusson and Riccardo Manenti
Superconducting Devices in Quantum Opics,
edited by H. R. Hadfield and G. Johansson
(Springer International Publishing, Cham, 2016) pp. 217-244

III **Surface acoustic wave unidirectional transducer for quantum applications**
Maria K. Ekström, Thomas Aref, Johan Runeson, Johan Björck, Isac Boström and Per Delsing
(submitted, arXiv:1611.06018)

Contents

Nomenclature

List of abbreviations

COM	Coupling of modes, theory used to simulate the response of a FEUDT
FEUDT	Floating electrode unidirectional transducer
FEUDT_i	Sample i, which is a delay line with two FEUDTs in either a Towards or an Away configuration.
GaAs	Gallium arsenide
IDT	Interdigital transducer
IDT_i	Sample i, which is a delay line with two IDTs
$LiNbO_3$	Lithium niobate
P-matrix	Three port scattering matrix, relating the voltage and current in the electric port and the incoming and outgoing waves in the two acoustic ports 1 and 2. In this thesis port 1 is defined to face into the delay line.
QED	Quantum electrodynamics
qubit	Quantum-bit
S-matrix	Multi port complex scattering matrix, here we use three ports where the incoming and outgoing waves are related for the electric port 3 and the two acoustic ports 1 and 2. In this thesis port 1 is defined to face into the delay line.
SAW	Surface acoustic wave
SQUID	Superconducting Quantum Interference Device
UDT	Unidirectional transducer

List of symbols

$1/Y_0$	Characteristic impedance
$1/Y_L$	Characteristic load impedance
α	COM transduction parameter per unit length
Δ	Superconducting gap
δ	Detuning from the wavenumber at center frequency
ϵ_0	Permittivity in vacuum

ϵ_∞	Effective dielectric permittivity
η	Metalization ratio
γ_{bs}	Loss due to beam steering
γ_{diff}	Loss due to diffraction
γ_{tot}	Total estimated propagation loss (γ_{prop}) and loss due to conversion in the wrong direction (γ_{D})
γ_{ue}	Loss that cannot be explained by directivity (γ_{D}) nor propagation loss (γ_{prop})
γ_{vis}	Loss due to viscous damping
Γ_{ac}	Acoustic coupling of the qubit to SAWs
γ_{air}	Attenuation due to air loading
γ_{att}	Attenuation coefficient
γ_{D}	Loss due to conversion into the wrong acoustic port (directive loss)
Γ_{el}	Electrical coupling between the qubit and the electric gate
γ_{prop}	Estimated loss during propagation in a delay line, includes loss due to diffraction (γ_{diff}), beam steering (γ_{bs}) and viscous damping (γ_{vis})
Γ_{tot}	Total coupling of the qubit, includes both Γ_{el} and Γ_{ac}
κ	COM reflection parameter per unit length
λ	Wavelength
λ_0	Wavelength at the center frequency of a transducer set by the length of one unit cell
$\mathcal{F}\left[\rho_f(k)\right]$	Fourier transform of the surface charge density when a voltage is applied to one electrode and all other electrodes are grounded
μ_0	Constant approximation of $E(f)$
ϕ	Surface potential, where $+$ denotes propagation to the right and $-$ denotes propagation to the left
Φ_0	Magnetic flux quantum
Φ_{ext}	External magnetic flux applied through the SQUID loop
a	Electrode finger width
$A(f)$	Superposition of the response from multiple electrodes
a_n	Net charge on electrode n
A_R	Effective reflection strength of waves from the reflection center
A_T	Effective transduction strength of waves from the transduction center
$B(x)$	Slowly varying amplitude of left propagating waves
$b(x)$	Wave amplitude for left propagating waves

$B[\mu s]$	Time delay causing a loss of -3 dB due to beam steering
$B_a(f)$	Acoustic susceptance in the circuit model for an IDT
$B_{aq}(f)$	Acoustic susceptance of a qubit transducer
C	Total capacitance of a qubit
$C(x)$	Slowly varying amplitude of right propagating waves
$c(x)$	Wave amplitude for right propagating waves
c_g	Unitless factor accounting for the geometry of the electrodes in a transducer
C_T	Capacitance of a transducer
C_l	COM capacitance per unit length
e	Elementary charge
$E(f)$	Response of each individual electrode in a transducer
E_C	Charging energy of a transmon (qubit if it can be considered a two level system)
E_J	Josephson energy a transmon (qubit if it can be considered a two level system)
f	Driving frequency
f_0	Center frequency of a transducer
f_{QDT}	Acoustic resonance frequency of a qubit set by the length of the unit cell of its transducer
f_{10}	Electric fundamental resonance frequency of a transmon (qubit if it can be considered a two level system)
$G_a(f)$	Acoustic conductance in the circuit model for an IDT
G_{a0}	Acoustic conductance at center frequency in the circuit model for an IDT
$G_{aq}(f)$	Acoustic conductance of a qubit transducer
h	Planck's constant
h_1	COM constant determined from boundary conditions
h_2	COM constant determined from boundary conditions
I	Current in transducer
I_C	Critical current of the two Josephson Junctions (weak barriers) in the SQUID
k	Wavenumber
K^2	Electromechanical coupling constant
k_0	Wavenumber at center frequency of a transducer
k_B	Boltzmann's constant
K_1	COM parameter determined from boundary conditions
K_2	COM parameter determined from boundary conditions

L	Propagation distance, separation between two transducers in a delay line
$L + N_p\lambda$	Propagation distance between the centers of the transducers
L_J	Nonlinear inductance of a SQUID
N	Number of electrodes per unit cell
N_{in}	Number of phonons converted from electrical power by a transducer
N_p	Number of unit cells of a transducer
n_t	Transit number
p	Electrode pitch, defined as the electrode finger width plus the separation between the electrodes
P_{gate}	Electric power sent to qubit via gate line
P_{in}	Incoming power
P_{SAW}	Power carried by a SAW
P_ν	Legendre function of order ν
R	Reflection response of a delay line including multiple transits
R_N	Normal resistance of the two Josephson Junctions (weak barriers) in the SQUID
s	Imaginary eigenvalues (per unit lenth) of COM differential equation
S_n	Induced surface charge when all electrodes in a unit cell of a transducer are shorted (also the floating electrodes)
S_{41}	Loss during the acoustic reflection
S_{43}	Loss during the conversion from electric signals to SAWs
S_{q11}	Scattering element for acoustic reflection of a qubit
S_{q31}	Scattering element for transduction of a qubit
T	Transmission through a delay line including multiple transits
V	Applied voltage
v_0	SAW speed on a metal free surface
v_m	SAW speed when the surface is covered by a metal sheet
W	Electrode overlap defining the SAW beam width
x_{RC}	Effective center of reflection for one unit cell in a transducer
x_{TC}	Effective center of transduction for one unit cell in a transducer
x_n	Position of electrode n
Y_{IDT}	Total admittance of an IDT in the circuit model
Y_{Q}	Total admittance of a qubit in the combined semi-classical and circuit model
$Max\ T$	Maximum transmission through the delay line

Chapter 1

Introduction

People can hear your voice because the pressure in your lungs vibrates your vocal cords, and this creates sound. Sound propagates in air as vibrations of pressure and density, and oscillates both in time and space. The oscillation in time (number of repeating events per unit time) sets the frequency. A human being can perceive frequencies between 20 Hz and 20 kHz. Sound can also propagate in liquids and solid as mechanical vibrations.

At a much higher frequency and in a much colder environment, small mechanical vibrations can be measured at the quantum level. This means that their physical properties need to be described by quantum mechanics. Typically, these systems consist of micro-scale mechanical beams and drums that are cooled down to such low temperatures that the thermal excitations of the mechanical vibrations are frozen out [1–4]. There are also different types of mechanical vibrations propagating on the surface of a chip. Such surface acoustic waves can be combined with superconducting circuits mimicking light interacting with atoms. That is the quantum mechanical system described in this thesis, with the ultimate goal of measuring quantum sound.

A quantum of sound is the minimum amount of mechanical vibration involved in an interaction and it is called a phonon. The analogue for light, or more generally electromagnetic radiation, is the photon. A physical property, such as the electromagnetic field or an atom can be quantized, which means that some property can only take certain discrete values. For instance, an electron in an atom can only exist at certain energy levels. When the atom interacts with light, it can get excited, *i.e.* an electron in the atom moves from one energy level to a higher one. After a while, the electron falls back to the lower energy level and the atom relaxes by emitting a single quantum, a photon in the case of light and a phonon in the case of sound.

Light interacting with matter is used to study physical properties in the field of quantum optics, where quantum mechanics is used to describe the dynamics of electromagnetic waves and atoms. In 2012, Serge Haroche and David Wineland were awarded The Nobel Prize in Physics for enabling measurements and manipulation of single ions [5, 6] and photon states [5, 7, 8] without destroying these quantum systems. Quantum optics was originally performed with natural atoms irradiated with optical light. To increase the interaction strength, the atoms are sometimes allowed to interact with electromagnetic fields confined in cavities, which is referred to as cavity quantum electrodynamics (cavity QED) [9]. In addition to the many possibilities with natural atoms, there are other systems that are used for studying quantum electrodynamics such a quantum dots [10], nitrogen-vacancy centers in diamond [11], rare-earth ions in crystals [12] and the most important ones for this thesis, superconducting circuits.

1.1 Superconducting artificial atoms

Artificial atoms can be made in superconducting circuits, where they can interact with electric microwave signals on chip. This version of quantum optics is know as circuit cavity QED if the interaction is with superconducting cavities [13, 14], or waveguide QED for interaction in open transmission lines [15–18].

A superconducting artificial atom is based on a nonlinear element together with traditional circuit elements, such as a capacitance. The nonlinearity is formed when a superconductor is interrupted with a thin insulating barrier, such that current can tunnel though it. The junction is called a Josephson junction [19] and its nonlinearity causes the energy levels of the artificial atom to be separated non-equidistantly, essentially perturbing the equal spacing of the energy levels for a simple harmonic oscillator. The transitions between these energy states define the frequencies at which the artificial atom can absorb and re-emit electromagnetic radiation, *i.e.* get excited by or emit photons. To enable tuning of the transition frequencies, two Josephson junctions can be used to interrupt a superconducting ring, which forms a Superconducting Quantum Interference Device (SQUID). If the transition between the two lowest energy levels can be addressed separately from higher energy levels, the artificial atom can be used as a quantum-bit (qubit).

Since superconducting circuits can be designed and fabricated with lithography processes to suit a certain experiment, they make it possible to study some unique physical phenomena and also combine different types of quantum systems. It is possible to design a superconducting artificial atom to interact with sound, or more specifically with propagating surface acoustic waves (SAWs) by placing it on a piezoelectric substrate. This was experimentally shown for the first time in appended Paper I and was inferred from measurements with a single electron transistor [20]. SAWs are mechanical vibrations propagating on the surface of solids, and they can be generated and detected with periodic structures of electrodes on piezoelectric substrates. The SAWs, their generation and detection as well as their interaction with a superconducting artificial atom will be described in Chapter 2 and is covered in appended Paper II.

SAWs can also be used in other quantum devices such as resonators [21, 22] (covered in appended Paper II), absorption in double quantum dots [23], transport of quantum information [24–26] and phonon assisted tunneling [27]. These advances have opened up new possibilities in a joint SAW and quantum research field. SAWs' five order of magnitude slower speed than light, makes their wavelength at microwave frequencies comparable to the wavelengths of optical light. This combined with the fact that many of the piezoelectric materials used for SAWs are also used in optics, raises the potential to connect microwave circuit QED with optical wavelength systems using SAW [28]. Building such hybrid systems to utilize the benefits and avoid the drawbacks present in different quantum research fields is of great interest [29, 30] and a universal theoretical platform has been developed to link a wide range of artificial atoms [31].

There are many possibilities with artificial atoms, and they can even reach regimes that are not possible with natural atoms. An example of this is the superconducting artificial atom in appended Paper I, which is twenty times larger than the wavelength of the field it interacts with and could easily have been made larger. Such as system cannot be treated as a point-like source, unlike known cases of both artificial and natural atoms interacting with light. The large artificial atom couples to SAWs in many points separated wavelengths apart and is theoretically predicted to have frequency-dependent coupling and energy levels due to interference effects caused by the many coupling points [32] (summarized in appended Paper II).

Although there are many physical phenomenas that are easier to study with superconducting artificial atoms than with natural atoms, there are also experiments that are more difficult to perform. One example is the detection of single propagating photons or phonons. In quantum optics, radiation can be characterized by the correlation of emitted photons in time using single photon detectors [33, 34]. These do not exist for microwave photons since microwaves have several orders of magnitude lower energy. Instead, the temporal correlation is made from measurements of the amplitude of the field [35–39]. To conduct a similar experiment with propagating SAW phonons, such a system would benefit from more efficient conversion between electric microwave signals and SAWs.

The improvement of this conversion has been studied extensively in classical SAW devices ever since the generation and detection of them was possible with the interdigital transducer (IDT) [40] on piezoelectric materials. Different types of materials, origins of losses and transducer types have been studied and characterized [41–45]. The transducers are engineered in many ways to suit various application, among those are the unidirectional transducers (UDTs) [42, 46]. UDTs have lower losses than IDTs because they can focus the SAWs in one direction rather than symmetrically in both directions, as happens in IDTs. Both UDTs and other types of transducers have been investigated for gigahertz frequencies [47], following the increasing frequencies used for telecommunications, and some experiments have utilized higher harmonics [48]. Although, it has been shown that the loss of the transducers reduces dramatically when they are superconducting [49], most of the studies with SAWs have been done at room temperature. Superconducting UDTs and IDTs are studied in appended Paper III to improve the conversion efficiency between electric microwave signals and SAWs at the quantum level.

The fabrication and measurement of the devices used in the appended papers, is covered in Chapter 3 and the results are discussed in Chapter 4. This is followed by a summary of the thesis and the appended papers together with future possibilities for detecting propagating SAW phonons in Chapter 5.

Chapter 2

Surface Acoustic Waves

Surface acoustic waves (SAWs) are mechanical vibrations elastically propagating along the surface of solids. They were first described by Lord Rayleigh in Ref. [50], and are important in many natural phenomenas, such as earthquakes. In earthquakes, they can destroy large land areas because they dissipate very little power into the bulk, allowing them to propagate very long distances. Although the low dissipation of the SAWs was found interesting, it was not until 80 years after their discovery that SAWs could be artificially generated on a piezoelectric material when the interdigital transducer (IDT) was introduced by White and Voltmer [51]. After this, many different designs followed, for instance with advanced features to shape the SAW pulse response or direct the SAW beam. Since piezoelectric materials' polarization charges are coupled to their particle displacements, electric power can be converted into SAW power and vice versa. This allows a variety of transducers to be incorporated as electric circuit elements, such as bandpass filters, resonators and delay lines. They are also very important in many commercial applications, for instance in TV and mobile technology.

Here, we will focus on the type of SAWs that can be described as pure Rayleigh waves. These waves are confined to the surface and decay exponentially in the bulk. This chapter aims to give a brief introduction to this type of SAWs, their motion and how they can be generated, which is explained in detail in [41–43]. A semi-classical approximation of a qubit coupled to surface acoustic waves will also be described, following the supplementary material in appended Paper I and II. For a full quantum model, the reader is referred to Refs. [32, 52] and the summarized version in appended Paper II. Later in this chapter, a type transducer generating SAWs in a preferred direction is discussed together with a more extensive model to describe its more complicated response.

2.1 Basic properties

When a SAW propagates, the material near the surface moves elliptically together with an electrostatic wave. The elliptic motion is produced from compression in the propagation direction and shearing in the direction normal to the surface [41]. Since the compressional motion dominates, the electrostatics can be described by an electric potential at the surface that only extends about a wavelength into the bulk. At the surface this potential can be expressed by

$$\phi(x,t) = |\phi| e^{j(2\pi f t - kx)} \tag{2.1}$$

for a SAW propagating along the x-axis at time t. $|\phi|$ is the magnitude of the wave at the surface and $k = 2\pi/\lambda$ is the wave vector for a wavelength λ of the SAW [43].

SAWs can propagate in any material and their speed is determined by the material properties. They can be generated on piezoelectric materials, which are usually anisotropic. For a given cut of an anisotropic crystal, there are only a few directions where the SAW will propagate without curving (known as beam steering) [41].

The cut and orientation also affects the piezoelectric properties of the substrate. The strength of the electromechanical coupling coefficient K^2 depends on how the strain and stress relate to the electric field, *i.e.* how the permittivity relates to the stiffness of the material, all of which can be orientation dependent. For SAWs, K^2 is approximated as the the change of speed when the SAW propagates under a metallized surface

$$K^2 = 2\frac{\Delta v}{v} = 2\frac{v_0 - v_m}{v_0}, \tag{2.2}$$

where v_0 is the speed of the SAW on a metal free surface and v_m is the speed when the surface is covered by a metal sheet [42]. K^2 is listed for some piezoelectric materials in Table 1 in appended Paper II. For example, the strong piezoelectric material lithium niobate, Y-cut with propagation in the Z-direction, has $v_0 = 3488$ m/s and $K^2 = 4.8$ % [42]. It is almost 70 times stronger than gallium arsenide, which has $K^2 = 0.07$ % on the (100) surface with a SAW traveling along the [011] at the speed of 2864 m/s [41].

Another important property for SAWs is the effective dielectric permittivity ϵ_∞ of both the material that the SAW propagates and the medium above. Permittivity relates the polarization charge to an applied electric field for any dielectric material and it is usually expressed in terms of the permittivity in vacuum ϵ_0. The effective dielectric permittivity is defined such that it expresses the capacitance per unit length between two electrodes on the surface of the piezoelectric material. For YZ lithium niobate the effective dielectric permittivity $\epsilon_\infty = 46\epsilon_0$, while it is $12\epsilon_0$ for gallium arsenide [41]. The effective dielectric permittivity is, in addition to the electromechanical coupling coefficient and SAW speed, listed for some piezoelectric crystals in Table 1 in appended Paper II. All of these properties are important to consider when generating and detecting SAWs.

2.2 Generation and detection

To generate a SAW, the simplest configuration is a single electrode IDT. The IDT consists of long electrodes in a periodic structure seen in Figure 2.1. All electrodes have the same finger width a, which is usually equal to the separation between them. The periodic structure can be divided into unit cells with length λ_0, where each unit cell has one electrode connected to the top bus and one connected to the bottom usually grounded bus.

When a voltage is applied over the IDT, an electric field is created between the electrodes connected to the top bus and the lower grounded bus. This creates strain in the underlaying piezoelectric material, which generates SAWs in both directions from

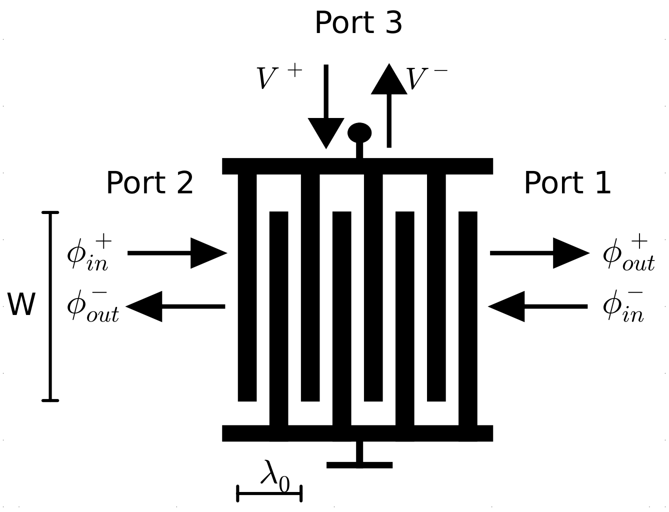

Figure 2.1: A single electrode IDT with four unit cells and an electrode overlap W. The unit cell has a length of λ_0, which defines the center frequency of the IDT. All electrodes are alternatively connected to the top live bus or the bottom grounded bus. Electric signals can be sent and detected via port 3, while port 1 and port 2 are acoustic ports.

each unit cell. The SAWs carry a total power

$$P_{\mathrm{SAW}} = |\phi|^2 \frac{W}{\lambda} \frac{2\pi\epsilon_\infty v_0}{K^2} = |\phi|^2 Y_0, \tag{2.3}$$

where W is the beam width set by the electrode overlap, $1/Y_0$ is the characteristic impedance from treating the IDT as a transmission line [41] and K^2 qualifies how much electric power can be converted to or from SAW power.

If the applied voltage V is on resonance with the center frequency of the IDT $f_0 = v/\lambda_0$, the contributions from all unit cells add in phase and a resonant SAW is emitted. The generated SAW has a surface potential $\phi = VE(f)A(f)$, which is the superposition of the response of each electrode $(E(f))$ and the superposition of multiple electrodes $(A(f))$ in a transducer. The response of one electrode is

$$E(f) = j\frac{K^2}{2\epsilon_\infty}\mathcal{F}\left[\rho_f(k)\right], \tag{2.4}$$

where $\mathcal{F}\left[\rho_f(k)\right]$ is the Fourier transform of the surface charge density when a voltage is applied to one electrode and all other electrodes are grounded. Since $E(f)$ is varying slowly with frequency, it is usually approximated with a constant $0.84jK^2$ for single electrode IDTs [42]. If the electrode spacing is equidistant such that $|x_n - x_{n-1}| = \lambda_0$, the superposition of multiple electrodes gives the array factor

$$A(f) = \sum_{n=1}^{N_p} e^{jkx_n} = \frac{\sin\left(N_p\pi\frac{f-f_0}{f_0}\right)}{\sin\left(\pi\frac{f-f_0}{f_0}\right)}, \tag{2.5}$$

for a driving frequency f and the position x_n of the live electrodes [42]. The strength of the SAW response increases with the number of unit cells N_p.

In the same way as the IDT emits SAWs, it can also detect them. The incoming SAW generates a current in the IDT

$$I = -2\phi E(f)A(f)Y_0, \tag{2.6}$$

which creates a voltage and in this way the incoming SAW is converted to electric signal.

2.2.1 Three port scattering matrices

The IDT in Figure 2.1 can be described by a complex scattering matrix with three ports; two acoustic ports (1 and 2) and one electric port (3)[†]. This scattering matrix relates the incoming and outgoing signals through

$$\begin{pmatrix} \phi_{out}^{+} \\ \phi_{out}^{-} \\ V^{-} \end{pmatrix} = \begin{pmatrix} S_{11} S_{12} S_{13} \\ S_{21} S_{22} S_{23} \\ S_{31} S_{32} S_{33} \end{pmatrix} \begin{pmatrix} \phi_{in}^{-} \\ \phi_{in}^{+} \\ V^{+} \end{pmatrix}, \tag{2.7}$$

where the signs represent the direction of the wave. Traditionally, + is towards the right for acoustic waves and towards the transducer for electric waves. Assuming energy conservation and reciprocity the complex scattering elements can be simplified to $S_{31} = S_{13}$ and $S_{32} = S_{23}$. If the transducer is symmetric, as in the case for the single electrode IDT, this can be further simplified to $S_{31} = S_{32}$, $S_{21} = S_{12}$ and $S_{11} = S_{22}$.

A more convenient scattering matrix for transducers is the P-matrix, where the voltage and current is related for the electric port. The P-matrix is defined as

$$\begin{pmatrix} \phi_{out}^{-} \\ \phi_{out}^{-} \\ I \end{pmatrix} = \begin{pmatrix} P_{11} P_{12} P_{13} \\ P_{21} P_{22} P_{23} \\ P_{31} P_{32} P_{33} \end{pmatrix} \begin{pmatrix} \phi_{in}^{+} \\ \phi_{in}^{-} \\ V \end{pmatrix}, \tag{2.8}$$

where P_{13} corresponds to how much electric signal is converted into acoustic signal per unit voltage and P_{33} is the IDT admittance. Similarly to the S-matrix, the P-matrix elements can be related; $P_{21} = P_{12}$, $P_{31} = -2P_{13}$ and $P_{32} = -2P_{23}$.

The elements of the two scattering matrices are related through

$$S_{11} = P_{11} - \frac{P_{13}P_{31}}{Y_L + P_{33}}, \qquad S_{22} = P_{22} - \frac{P_{23}P_{32}}{Y_L + P_{33}}, \tag{2.9a}$$

$$S_{12} = P_{12} - \frac{P_{13}P_{32}}{Y_L + P_{33}}, \qquad S_{21} = P_{21} - \frac{P_{23}P_{31}}{Y_L + P_{33}}, \tag{2.9b}$$

$$S_{13} = \frac{2\sqrt{Y_L}P_{13}}{Y_L + P_{33}}, \qquad S_{31} = \frac{2\sqrt{Y_L}P_{31}}{Y_L + P_{33}}, \tag{2.9c}$$

$$S_{23} = \frac{2\sqrt{Y_L}P_{23}}{Y_L + P_{33}}, \qquad S_{32} = \frac{2\sqrt{Y_L}P_{32}}{Y_L + P_{33}}, \tag{2.9d}$$

$$S_{33} = \frac{Y_L - P_{33}}{Y_L + P_{33}}, \tag{2.9e}$$

where $1/Y_L$ is the characteristic load impedance, usually $50\,\Omega$ [42].

[†]Note the different notation in appended Paper 1, where port 1 is the electric port, 3 is the acoustic port facing the qubit and 2 is the other acoustic port.

2.3 Delay line: propagation between two transducers

Since transducers are both emitters and receivers of SAWs, they are commonly configured in a delay line. The name comes from the use of delay lines in electric circuits, where they delay the signal the amount of time it takes the five order of magnitude slower SAW to propagate. A delay line has two transducers separated a certain distance L on the piezoelectric substrate. If we assume that port 1 of both transducers face into the delay line, *i.e.* towards each other, the electric signal is converted into SAWs via the scattering element S_{31}. The SAWs propagate through the delay line to the transducer on the other side, where they are partly converted back to electric signal via S_{13} and partly acoustically reflected back into the delay line via S_{11}.

The response of the delay line can be measured via the electric port of each transducer. For two identical transducers multiple transitions interfere and the measured electric reflection follows

$$R = S_{33} + \sum_{n_t=1}^{\infty} S_{13}^2 S_{11}^{2n_t-1} e^{-j2n_t kL} = S_{33} + S_{13}^2 \frac{S_{11} e^{-j2kL}}{1 - S_{11}^2 e^{-j2kL}} \tag{2.10}$$

where kL is the phase the SAW picks up every time it propagates the delay line, n_t is the number of transits and the scattering elements are found from Eq. (2.7). The main electric reflection includes no SAW transits and follows S_{33}. For a multiple transiting SAW the measured transmission follows

$$T = \sum_{n_t=1}^{\infty} S_{13}^2 S_{11}^{2(n_t-1)} e^{-j2n_t kL} = S_{13}^2 \frac{e^{-jkL}}{1 - S_{11}^2 e^{-j2kL}}, \tag{2.11}$$

The main transmission of the delay line is the first transit, *i.e.* the SAWs propagates once through the delay line and $n_t = 1$.

2.4 Double electrode interdigital transducers

The single electrode IDT introduced in Section 2.2 (Figure 2.1) has the most straightforward electrode configuration but it suffers from internal mechanical reflections. Another type of IDT with a simple electrode configuration, which does not suffer from internal mechanical reflections, is the double electrode IDT [53] in Figure 2.2a. Instead of two electrodes per unit cell, it has four: two connected to the upper live bus and two connected to the bottom grounded bus. Each electrode connected to the upper bus emits a SAW in two directions. If the SAW is emitted at center frequency from electrode n, it propagates the distance $\lambda_0/2$ from and back to electrode n when it is reflected by electrode $n-1$. This corresponds to a phase shift of π, which means that the reflected SAW interferes destructively with the wave emitted by electrode n in the other direction. Thus, internal mechanical reflections can be neglected for double electrode IDTs close to center frequency at the cost of twice smaller lithography than the single electrode IDT. By ignoring internal mechanical reflections, the simplified response can be described by a basic SAW circuit model.

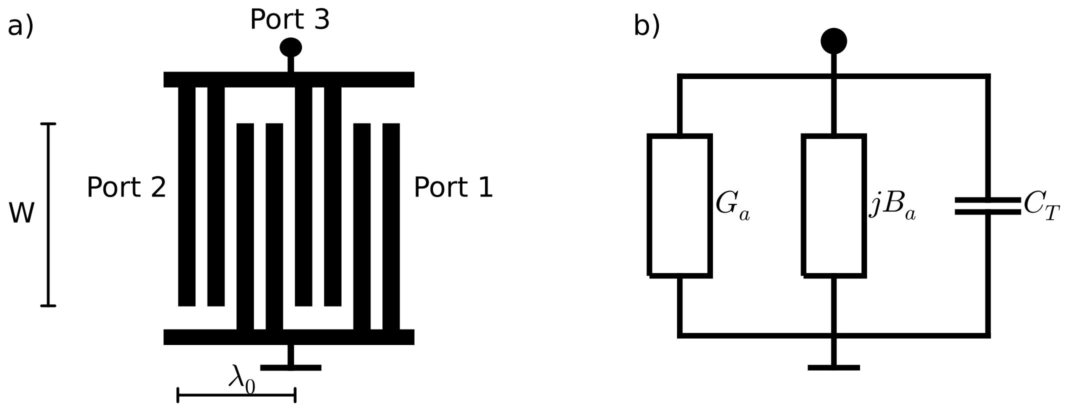

Figure 2.2: a) Double electrode IDT with electrode overlap W and unit cell length λ_0. Each unit cell has four electrodes, which makes it possible to ignore internal mechanical reflections (see text). b) The equivalent circuit of a double electrode IDT includes an acoustic conductance $G_a(f)$, an acoustic susceptance $B_a(f)$ and an electrode capacitance C_T.

2.4.1 Circuit model

The circuit model described here is a simple SAW circuit model, assuming no mechanical reflections and no loss, and it is valid for double electrode IDTs. It can also be used to approximate single electrode IDTs with few unit cells. For a more detailed description, the reader is referred to appended Paper II and literature such as Rafs. [40–42].

In the circuit model the IDT is approximated with an acoustic conductance $G_a(f)$, an acoustic susceptance $B_a(f)$ (Hilbert transform of $G_a(f)$) and a capacitance C_T (Figure 2.2b). The equivalent circuit has a total admittance $Y_{\mathrm{IDT}}(f) = G_a(f)+jB_a(f)+j\omega C$ with $\omega = 2\pi f$. These circuit elements can be calculated from the SAW theory in Section 2.2 as

$$G_a = 2|E(f)A(f)|^2 Y_0 \approx G_{a0}\left[\frac{\sin(X)}{X}\right]^2 \tag{2.12a}$$

$$B_a \approx G_{a0}\frac{\sin(2X)-2X}{2X^2} \tag{2.12b}$$

$$C_T \approx \sqrt{2}N_p W \epsilon_\infty, \tag{2.12c}$$

where $X = \pi N_p(f-f_0)/f_0$ for a driving frequency f close to f_0. $A(f)$ is evaluated from Eq. (2.5) with x_t at the center of the two live electrodes and the slowly varying $E(f)$ is approximated with a constant $\mu_0 = c_g jK^2$ with $c_g = 0.62$ for double electrode IDTs [42]. From this the acoustic conductance at center frequency $G_{a0} = 4\cdot c_g^2 2\pi f_0 \epsilon_\infty N_p^2 W K^2$.

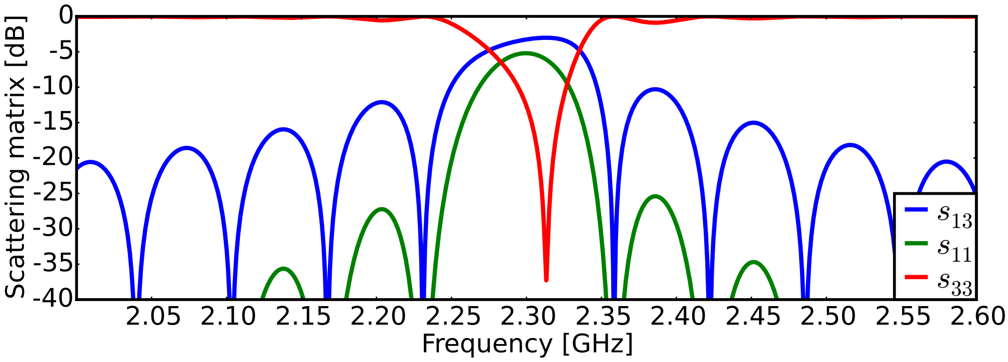

Figure 2.3: Three port scattering elements S_{13} (blue), S_{11} (green) and S_{33} (red), calculated from the circuit model for a double electrode IDT with 36 unit cells and 46 μm electrode overlap.

Using this model, we can calculate the elements of the three-port scattering matrix in Eq. (2.7) as

$$S_{11} = S_{22} = -\frac{G_a}{Y_{\mathrm{IDT}}(\omega) + Y_L} e^{-jN_p\lambda_0}, \tag{2.13a}$$

$$S_{13} = S_{23} = \frac{j\sqrt{2G_a Re(Y_L)}}{Y_{\mathrm{IDT}}(\omega) + Y_L} e^{-jN_p\lambda_0/2} \text{ and} \tag{2.13b}$$

$$S_{33} = \frac{Y_L - Y_{\mathrm{IDT}}(\omega)}{Y_L + Y_{\mathrm{IDT}}(\omega)} \tag{2.13c}$$

for a double electrode IDT with wavelength λ_0 at center frequency and hence a transducer length of $N_p\lambda_0$. The scattering parameters for a double electrode IDT with 36 number of unit cells and an electrode overlap of 46 μm is shown in Figure 2.3. The electric/SAW conversion (parameter S_{13}) is limited to a maximum of -3 dB, because IDTs have symmetric conversion into both acoustic ports. In a delay line geometry, this means that only 50 % of the power propagates in the right direction towards the other IDT. Due to reciprocity, the theoretical minimum insertion loss of a delay line with symmetric IDTs is -6 dB.

The electric reflection (parameter S_{33}) from any transducer is optimal when the transducer is impedance matched to outside electronics. The impedance matching is roughly met by designing the real part of $1/Y_{\mathrm{IDT}}$, *i.e.* G_{a0}, to be 50 Ω close to frequency where B_a cancels C_T. Thence, there are a few design and a few substrate material parameters that can be used to control G_{a0}. The design parameters can be limited by the size of the substrate and the fabrication, *i.e.* the number of unit cells cannot be too many and the electrode overlap cannot be too large. A material with a higher electromechanical coupling and a higher effective dielectric constant requires fewer unit cells, such as lithium niobate in comparison to gallium arsenide.

For a fixed number of unit cells the bandwidth can be approximated with $0.9f_0/N_p$ [41]. Accordingly, the bandwidth of the double electrode IDT in Figure 2.3 is 60 MHz, but the transducer can emit and pick up signal outside this band. In addition, the SAW emission and pick up is wider in frequency than both the acoustic reflection (parameter

S_{11}) and the electric reflection (Figure 2.3).

In conclusion, to optimize an IDT the electrode configuration and the impedance matching should be considered. The IDT should be designed such that the bandwidth is sufficient for the given experiment. Therefore, the number of unit cells can be balanced with the choice of the piezoelectric substrate for optimal electric/SAW conversion. Nevertheless, symmetric IDTs are limited by the theoretical minimum insertion loss of -3 dB which should be considered when designing the experiment.

2.5 Artificial atom coupled to surface acoustic waves

SAWs were treated purely classically in the previous sections. In this section, we discuss how SAWs are interacting with an artificial atom and the interaction will be treated semi-classically following appended Paper I and II.

An artificial atom has discrete energy states spaced non-equidistantly. They are commonly used in superconducting circuits to explore fundamental phenomena in quantum physics [14, 18]. In these circuits, the transition frequencies between the energy states in the artificial atoms are typically designed to be in the microwave range. In appended Paper I and II, the artificial atom in the superconducting circuit is not only interacting with electromagnetic microwaves but is even more strongly coupled to propagating SAWs.

To design an artificial atom to couple to SAWs, the similarities between the IDT electrode structure and the shunt capacitance used in transmons [54] can be exploited. In a transmon, the large capacitance shunts a Superconducting Quantum Interference Device (SQUID). The SQUID is a superconducting loop interrupted with two weak barriers, which separates the loop into two islands. One island is connected to an electrode on the top bus of the IDT and the other island is connected to the bottom grounded bus (Figure 2.4a).

The SQUID acts as a nonlinear inductor, which can be tuned by applying a magnetic field. The nonlinear inductance

$$L_J = \frac{\hbar}{2eI_C|\cos(\pi\Phi_{\text{ext}}/\Phi_0)|}, \tag{2.14}$$

where Φ_{ext} is the external magnetic flux applied through the SQUID loop, $\Phi_0 = h/(2e)$ is the magnetic flux quantum, e is the elementary charge and h is Planck's constant. The critical current $I_C = \pi\Delta/(2eR_N)$ and is limited by the choice of the normal resistance R_N of the two SQUID barriers. Δ is the BCS superconducting gap and it is 200 ueV for thin film aluminum, which has a critical temperature of $\sim$1.3 K.

Semi-classically, the artificial atom is treated as a two-level system, which is valid for energies low enough to never excite the artificial atom beyond the first excited energy state. At these levels, the artificial atom be called a quantum-bit (qubit) coupling to SAWs and the equivalent circuit of the qubit can be obtained adding L_J in parallel to the equivalent circuit of the IDT described in Section 2.4.1. The equivalent circuit of the qubit, illustrated in Figure 2.4b, has a total admittance of $Y_Q(f) = G_{aq} + jB_{aq} + j\omega C + 1/(j\omega L_J)$.

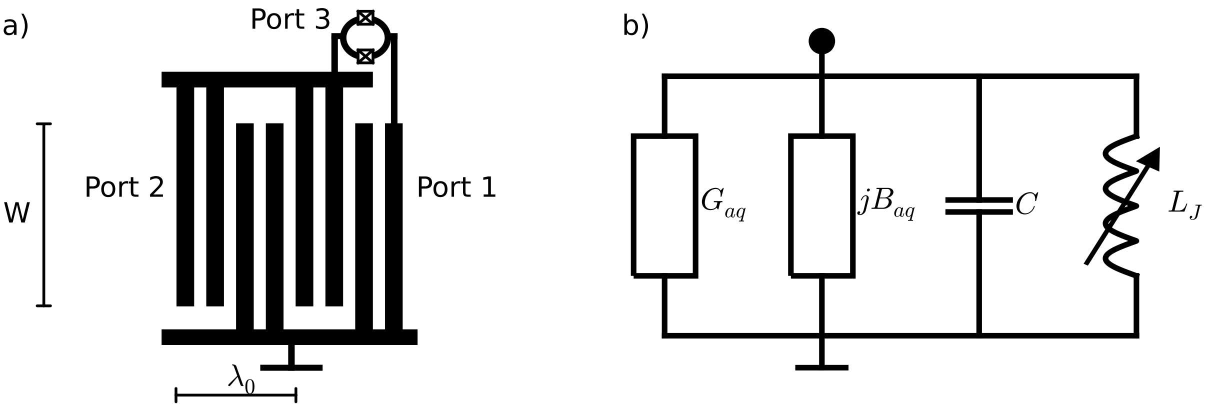

Figure 2.4: a) A transmon coupled to SAW through a double electrode IDT as its shunt capacitance. The top bus of the IDT is connected to one of the islands in the SQUID and the bottom grounded bus is connected to the other island. b) Circuit model of an artificial atom coupled to SAWs. The SQUID is treated as a tunable inductor in parallel to the equivalent circuit of the IDT in Figure 2.3b.

G_{aq} and B_{aq} describe the IDT structure and C is the total capacitance of the qubit. They can be calculated according to Eq. (2.12).

The qubit coupled to SAWs has two resonance frequencies, one acoustic f_{QDT} defined by the spacing of the IDT structure and one electric $f_{10}(\Phi_{\mathrm{ext}})$ that can be tuned by adjusting $L_J(\Phi_{\mathrm{ext}})$. The electric resonance frequency is described by the energy transition between the first excited state and the ground state $f_{10} = (E_1 - E_0)/h$, which for a transmon can be expressed as $f_{10}(\Phi_{\mathrm{ext}}) = (\sqrt{8E_J(\Phi_{\mathrm{ext}})E_C} - E_C)/h$. Where the charging energy is $E_C = e^2/(2C)$, and the Josephson energy is

$$E_J(\Phi_{\mathrm{ext}}) = \frac{\hbar^2}{(2e)^2 L_J(\Phi_{\mathrm{ext}})} = \frac{\hbar\pi\Delta}{4e^2 R_N}\left|\cos\left(\frac{\pi\Phi_{\mathrm{ext}}}{\Phi_0}\right)\right| = E_{\mathrm{J,max}}\left|\cos\left(\frac{\pi\Phi_{\mathrm{ext}}}{\Phi_0}\right)\right|. \tag{2.15}$$

There are three main characteristics that are important to consider for the qubit design: the anharmonicity, the coupling strength to the SAW and the coupling bandwidth. The anharmonicity is a measure of the nonlinearity of the artificial atom and describes how much the transition frequencies from the higher levels deviates from the fundamental resonance frequency. Generally the anharmonicity for transmons is $-E_C$, but when it is coupled to SAW it is also affected by a Lamb shift of the size of $-B_{aq}(f)/(2\pi C)$ originating from the IDT. This Lamb shift is briefly discussed in the supplementary material of appended Paper I and in appended Paper II, and is further explained in Refs. [32, 52].

The anharmonicity needs to be bigger than the qubit coupling to facilitate treatment of the qubit as a two-level system. The coupling of the qubit to SAWs is the rate at which energy stored in the qubit converts into SAWs by relaxation, dissipating power into the real part of the admittance. At coinciding acoustic and electric resonance $f_{\mathrm{QDT}} = f_{10} = 1/\sqrt{L_J C}$, it can be expressed as

$$\Gamma_{\mathrm{ac}} = \frac{G_{a0}}{2C} \approx 0.5 \cdot 2\pi f_{\mathrm{QDT}} K^2 N_p \tag{2.16}$$

for a qubit with a double electrode IDT. Note that the coupling is proportional to N_p, while the anharmonicity is inversely proportional to N_p. This needs to be considered when a qubit is designed for SAW experiments, such as in appended Paper I.

When the qubit is placed close to a classical IDT, the emitted SAWs from the qubit can be detected. The signal from the qubit to the IDT follows Eq. (2.11), but now the transducers are not equal and the scattering elements are different. If we denote the scattering element for the electric to SAW conversion in the qubit S_{q31} and the acoustic reflection by the qubit S_{q11}, multiple transits in the SAW device interfere as

$$R = \frac{S_{q31} S_{13} e^{kL}}{1 - S_{11} S_{q11} e^{j2kL}}, \tag{2.17}$$

where the scattering parameters for the IDT are described in Section 2.4.1. The qubit scattering elements are evaluated using the reflection of photons from a qubit [55] and by assuming that SAW phonons are reflected in a similar way. To approximate S_{q11}, the qubit is excited by the IDT. The number of phonons converted in the IDT from electrical power is $N_{\mathrm{in}} = P_{\mathrm{in}} |S_{13}|^2/(hf)$. Since part of the phonons can be reflected by the qubit, they can transit betwen the qubit and the IDT multiple times and the total number of phonons reaching the qubit is

$$N_{\mathrm{in}} \approx \frac{P_{\mathrm{in}}}{hf} \left| S_{13} \sum_{n_t=0}^{\infty} (S_{11} S_{q11} e^{2jkL})^{n_t} \right|^2 = \frac{P_{\mathrm{in}}}{hf} \left| \frac{S_{13}}{1 - S_{11} S_{q11} \exp(2jkL)} \right|^2. \tag{2.18}$$

For S_{q31}, the qubit is assumed to be excited with photons from the gate. These approximations give

$$S_{q11} \approx -\frac{1 - 2j \frac{f_{10} - f}{\Gamma_{\mathrm{tot}}}}{1 + 4\left(\frac{f_{10}-f}{\Gamma_{\mathrm{tot}}}\right)^2 + 4\frac{N_{\mathrm{in}}}{\Gamma_{\mathrm{tot}}} \left| \frac{1 - S_{11} S_{q11} \exp(2jkL)}{S_{13}} \right|^2}, \tag{2.19a}$$

$$S_{q31} \approx \sqrt{\frac{2\Gamma_{\mathrm{ac}}\Gamma_{\mathrm{el}}}{\Gamma_{\mathrm{tot}}}} \frac{1 + \frac{2j(f_{QDT} - f)}{\Gamma_{\mathrm{tot}}}}{1 + \left(\frac{4(f_{QDT}-f)}{\Gamma_{\mathrm{tot}}}\right)^2 + \frac{8\Gamma_{\mathrm{el}}}{\Gamma_{\mathrm{tot}}^2} N_{in}}, \tag{2.19b}$$

where Γ_{el} is the electric coupling and $\Gamma_{\mathrm{tot}} = \Gamma_{\mathrm{el}} + \Gamma_{\mathrm{ac}}$. f is the driving frequency for the electric excitation, and for convenience f_{QDT} is the coinciding electric and acoustic resonance. A derivation of S_{q11} and S_{q31} can be found in the supplementary material of appended Paper I. The scattering elements of the qubit are power dependent and decrease for increasing excitation power, but the expressions in Eq. (2.19) are only valid for low enough powers such that the artificial atom can be treated as a two-level system.

2.6 Floating electrode unidirectional transducer

When SAWs are used to carry quantum information, it is important to have low losses and efficient electric/SAW conversion. The conversion in the IDTs in Section 2.4 is symmetric for both acoustic ports, and hence 50 % of the acoustic power is lost in the wrong direction.

Unlike the symmetric IDT, a unidirectional transducer (UDT) [42, 46] can be optimized to release most of its SAW energy in one preferred direction. This can be done by maximizing the scattering element S_{13} while minimizing S_{23} in Eq. (2.7) in Section 2.2.1. UDTs have previously been studied for classical applications, such as low-loss SAW filters at room temperature [41, 42]. Since they have complicated structures, a substantial effort has been made in engineering low loss UDTs at gigahertz frequencies [47]. Various types of UDTs have been tested for different piezoelectric substrates. On strong piezoelectric materials, such as lithium niobate, the preferred UDT types utilize piezoelectric reflections, because these reflections dominate over mechanical reflections.

Here we focus on one type of UDT utilizing piezoelectric reflections [56], which is based on a floating electrode unidirectional transducer (FEUDT) [57] (Figure 2.5). It consists of a periodic structure, where a unit cell has six electrodes with the same width and electrode separation. Each unit cell has one electrode connected to the live upper bus, one electrode connected to the lower grounded bus and four floating electrodes, two of which are connected to each other. The design is such that electric/SAW conversion is optimized for port 1 and minimized for port 2.

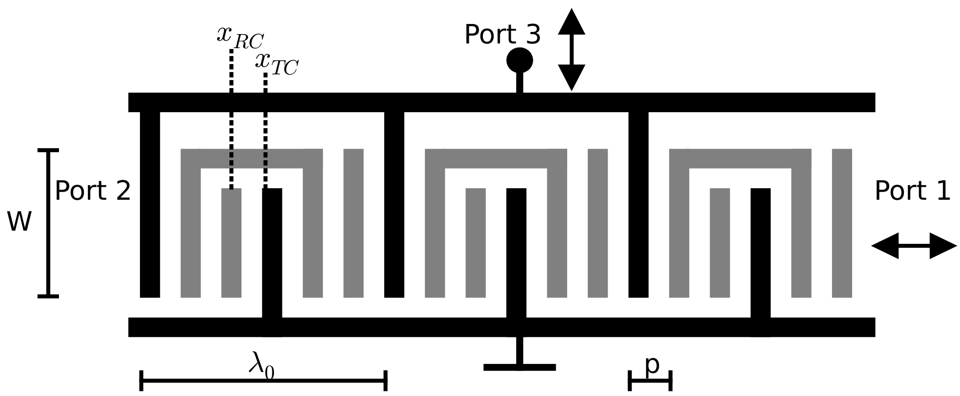

Figure 2.5: A FEUDT with six electrodes in one unit cell. Each unit cell has a transduction center x_{TC} which is separate from its reflection center x_{RC}. The preferred electric/SAW conversion is towards the right [57], in port 1. The upper bus is connected to live electrodes, the lower bus is grounded and two of the floating electrodes (gray) are connected to each other. The length of one unit cell is λ_0 and the overlap of the electrodes is W. All electrodes have the same finger width a, which is equal to the separation between them, and has a pitch $p = 2a$, such that $a = \lambda_0/12$.

The ratio between the power converted to port 1 and 2, defines the directivity of the FEUDT. The directivity of each unit cell can be illustrated by a spatially separated center of transduction x_{TC}, where the SAWs are regarded to be generated, and a center of reflection x_{RC}, where the SAWs are regarded to be reflected. Both centers, shown in Figure 2.5, can be found by the Coupling of Mode theory in the following section. The spatial separation of these centers, results in constructively and destructively interfering SAWs in the direction of port 1 and port 2, respectively.

2.6.1 Coupling of modes

To describe transducers that are more complicated than the double electrode IDT, such as FEUDTs, internal mechanical reflections need to be considered. Here, this is done with the coupling of modes (COM) theory [42, 58–62], which involves coupling between waves propagating in the same or opposite directions and a distributed transduction. This method does not include bulk waves, diffraction nor beam steering. The resistivity of the electrodes and buses are also ignored, which is an accurate assumption for our superconducting circuits. In the derivation of the COM equations, it is also assumed that reflection and transduction of the transducer can be treated separately and then added. The current in the transducer is calculated for a shorted transducer for left propagating waves and for right propagating waves, and the contribution from the capacitance when $V \neq 0$ is added. First COM will be described for a general periodic transducer and then the COM parameters for a FEUDT will be found from a quasi-static approximation.

Following Morgan [42], we consider left propagating waves with amplitude $b(x)$, and right propagating waves with amplitude $c(x)$ (Figure 2.6). Using the wavenumber at the center frequency k_0, slowly varying amplitudes can be defined as $B(x) = b(x)e^{-jk_0x}$ and $C(x) = c(x)e^{jk_0x}$ such that the power of the waves are $|B(x)|^2/2$ and $|C(x)|^2/2$. A periodic transducer can then be described with the differential equations:

$$\frac{d}{dx}\begin{pmatrix} C(x) \\ B(x) \end{pmatrix} + \begin{pmatrix} j\delta & -\kappa \\ -\kappa^* & -j\delta \end{pmatrix}\begin{pmatrix} C(x) \\ B(x) \end{pmatrix} = V\begin{pmatrix} \alpha \\ \alpha^* \end{pmatrix} \tag{2.20a}$$

$$\frac{d}{dx}I(x) = 2\alpha^* C(x) - 2\alpha B(x) + j\omega C_l V, \tag{2.20b}$$

where $\delta \equiv k - k_0$ is the detuning from the wavenumber at the center frequency, κ is a reflection parameter per unit length, α is a transduction parameter per unit length and C_l is the capacitance per unit length. Eq. (2.20a) described the change in a SAW over a unit distance by combining reflected, transmitted and transduced waves. The solution is the sum of the complementary solution for $V = 0$ (shorted IDT), and the particular solution for $V \neq 0$. The matrix has eigenvalues $\pm js$, where $s^2 = \delta^2 - |\kappa|^2$, such that $B(x)$ and $C(x)$ are proportional to e^{jsx}. At frequencies close to the center frequency $|\delta| < |\kappa|$, s is imaginary and the complete solution to Eq. (2.20a) is

$$C(x) = h_1 e^{-jsx} + h_2 e^{jsx} + K_1 V, \tag{2.21a}$$

$$B(x) = h_1 p_1 e^{-jsx} + h_2 p_2 e^{jsx} + K_2 V. \tag{2.21b}$$

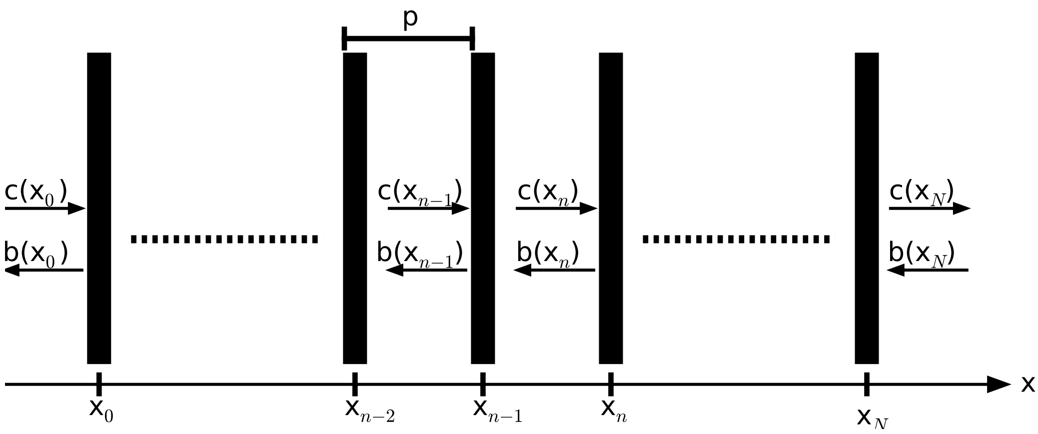

Figure 2.6: SAW amplitudes $b(x)$ and $c(x)$ propagating towards the left and right, respectively, in a transducer with N electrodes.

h_1 and h_2 are constants dependent on the boundary conditions;

$$p_1 = j(\delta - s)/\kappa \tag{2.22a}$$
$$p_2 = j(\delta + s)/\kappa \tag{2.22b}$$
$$K_1 = (\alpha^* \kappa - j\delta\alpha)/s^2 \tag{2.22c}$$
$$K_2 = (\alpha\kappa^* + j\delta\alpha^*)/s^2. \tag{2.22d}$$

Using the boundary conditions in Eq. (2.22) for the solution in Eq. (2.21), the elements in the P-matrix in Eq. (2.8) in Section 2.2.1 can be determined to be

$$P_{11} = \frac{-\kappa^* \sin(sN_p\lambda_0)}{s\cos(sN_p\lambda_0) + j\delta\sin(sN_p\lambda_0)} \tag{2.23a}$$
$$P_{12} = P_{21} = \frac{se^{-jk_0N_p\lambda_0}}{s\cos(sN_p\lambda_0) + j\delta\sin(sN_p\lambda_0)} \tag{2.23b}$$
$$P_{22} = \frac{\kappa\sin(sN_p\lambda_0)e^{-2jk_0N_p\lambda_0}}{s\cos(sN_p\lambda_0) + j\delta\sin(sN_p\lambda_0)} \tag{2.23c}$$
$$P_{31} = -2P_{13} = \frac{2\alpha^*\sin(sN_p\lambda_0) - 2sK_2(\cos(sN_p\lambda_0) - 1)}{s\cos(sN_p\lambda_0) + j\delta\sin(sN_p\lambda_0)} \tag{2.23d}$$
$$P_{32} = -2P_{23} = e^{-jk_0N_p\lambda_0}\frac{-2\alpha\sin(sN_p\lambda_0) - 2sK_1(\cos(sN_p\lambda_0) - 1)}{s\cos(sN_p\lambda_0) + j\delta\sin(sN_p\lambda_0)} \tag{2.23e}$$
$$P_{33} = -K_1P_{31} - K_2P_{31}e^{jk_0N_p\lambda_0} + 2(\alpha^*K_1 - \alpha K_2)N_p\lambda_0 + j\omega C_l N_p\lambda_0, \tag{2.23f}$$

where $N_p\lambda_0$ is the length the transducer. The P-matrix can be converted into the S-matrix using equation 2.9 in Section 2.2.1, and hence, by determining κ, α and C_l the scattering parameters of the device can be described.

2.6.2 Quasi-static approximation to find COM parameters for a FEUDT

To determine the COM parameters for a FEUDT, we follow the quasi-static approximation [59–61]. This is an easier approach than the comprehensive algebraic analysis in Ref. [58]. It is a simplified version of Green's function analysis, where the electrostatic and acoustic contributions are separated. It is assumed that the only waves present are non-leaky waves and that the velocity change caused by the mechanical and electrical loading are negligible. Further, the transducer is assumed infinitely periodic with constant electrode width and separation and each unit cell is evaluated separately. This is later extended to a transducer with a finite length neglecting edge-effects.

When a voltage is applied over a FEUDT with the length of one unit cell, a SAW is emitted with a surface potential described in Section 2.4. In that section the superposition of the response from one electrode in Eq. (2.4) was approximated as a constant, but $\mathcal{F}\left[\rho_f(k)\right]$ varies slowly. Here it is used to calculate the COM capacitance, transduction and reflection parameter. The Fourier transform of the surface charge density when a voltage is applied to one electrode and all other electrodes are grounded is expressed as

$$\mathcal{F}\left[\rho_f(k)\right] = \epsilon_\infty \frac{2\sin(\pi s)}{P_{-s}(-\cos(\pi\eta))} P_\nu(\cos(\pi\eta)), \tag{2.24}$$

where ν is the integer of $kp/(2\pi)$ and $s = kp/(2\pi) - \nu$ [42]. P_ν is the Legendre function of order ν and $\eta = a/p$ is the metalization ratio between the electrode width a and the electrode pitch p (defined as the width plus the separation). For the FEUDT, we assume equal electrode width and separation and hence $\eta = 1/2$. At center frequency $\lambda_0 = Np$, for N electrodes per unit cell and $k_0 = 2\pi/(Np)$, then ν is an integer of $1/N$.

It should be noted that the surface potential is derived from Green's function analysis. During the derivation, piezoelectricity is ignored with the result that a shorted array of electrodes does not reflect SAWs. This is not true, but the approximation is valid for transducers that only reflect weakly when shorted. For FEUDTs on $LiNbO_3$ the piezoelectric reflections are dominating and thus, the approximation of the surface potential can be used to determine their COM parameters [61].

Capacitance per unit length

First the capacitance per unit length is calculated. When a unit voltage is applied to one electrode per unit cell, surface charges are induced. This results a net charge

$$a_{n+1} = \frac{2\epsilon_\infty}{N} \sum_{i=0}^{N} \frac{\sin(\pi\nu)\cos(2\pi n\nu)}{P_{-\nu}(-\cos(\pi\eta))} P_{-\nu}(\cos(\pi\eta)), \tag{2.25}$$

on electrode $n+1$, where $\nu = i/N$. By superposing a_n, the net charges on each electrode in the unit cell can be determined for arbitrary voltages. These voltages are determined from electrostatic boundary conditions where live electrodes are allowed to have charge, while the charge on grounded and floating electrodes is zero. In addition, connected floating electrodes have the same voltage [61].

When both the voltages and the net charges on each electrode are determined, the capacitance per unit cell and aperture is obtained from the sum of the net charges on electrodes connected to the live bus. Accordingly, the COM parameter capacitance per unit length is found as

$$C_l = \frac{5\epsilon_\infty W}{8\lambda_0} \tag{2.26}$$

for a FEUDT with six electrodes per unit cell .

The above calculations are purely electrostatic and the substrate does not need to be piezoelectric. Piezoelectricity is introduced in order to find the two COM parameters for transduction and reflection.

Transduction

Secondly, the transduction parameter is evaluated while reflections are ignored. By applying an arbitrary voltage V_n on electrode n, SAWs arise with a surface potential ϕ described in Section 2.4 and with $\mathcal{F}\left[\rho_f(k)\right]$ from Eq. (2.24). The SAWs propagating to the right (ϕ^+) and to the left (ϕ^-) are the same except for the reversed sign of the exponent. By calculating the waves that leave each unit cell, a reference point can be found where the waves generated in both directions have the same amplitude and phase. This reference point is called the transduction center (Figure 2.5). From this center the waves have an effective transduction strength A_T, such that $\phi^{\pm}(0) = jA_T e^{\pm jk_0 x_{TC}}$ [61].

The electric to SAW transduction from port 3 to 1 is described by $P_{13} = \phi^-_{\mathrm{out}}/V$ in Eq. (2.8) in Section 2.2.1, and the amplitude of the outgoing SAW is such that $|\phi^-_{\mathrm{out}}|^2/2 = P_{\mathrm{SAW}}$, with P_{SAW} expressed in Eq. (2.3).

In addition, P_{13} is found from Eq. (2.23d). At at center frequency ($\delta = 0$), $P_{13} \approx -\alpha^*\lambda_0$ for a transducer with the length of one unit cell, *i.e.* the wavelength λ_0, and if $|\kappa|\lambda_0$ is assumed to be small and constant. By equating the two expressions for P_{13}, the transduction parameter per unit length is found from

$$\alpha = j\frac{A_T}{\lambda_0}\sqrt{Y_0}e^{jk_0 x_{TC}}. \tag{2.27}$$

Reflection

Finally, the reflection parameter is evaluated when the unit cell of the FEUDT is shorted. When all electrodes (including the floating electrodes) are considered shorted, an incoming SAW with ϕ_{in} give rise to induced surface charge

$$S_n = -\epsilon_\infty \phi_{\mathrm{in}}(0)\frac{\pi}{N}\left(\frac{P_\nu(-\cos(\pi\eta))P_{-\nu}(\cos(\pi\eta))}{P_{-\nu}(-\cos(\pi\eta))} + P_\nu(\cos(\pi\eta))\right)e^{-j2\pi(n-1)/N}, \tag{2.28}$$

on electrode n [59]. Here $\nu = 1/N$ and $\phi_{\mathrm{in}}(0)$ is a constant describing the amplitude of the incoming wave.

By allowing the floating electrodes to have nonzero voltages, charges are introduced in addition to S_n. These charges are introduced such that the total net charge on the floating electrodes is zero. From this, the net charge is used to determine the voltages of each electrode, using the same type of boundary conditions as for the calculation of the COM capacitance parameter [61].

The voltages on the electrodes generate a SAW, and once again we use the surface potential described in Section 2.4 and with $\mathcal{F}\left[\rho_f(k)\right]$ from Eq. (2.24). With the same argument as for the transduction, a reflection center x_{RC} (Figure 2.5) and an effective reflection strength A_R are found. Using these, the reflection coefficient $R^{\dagger} = \phi^{\pm}(0)/\phi_{\mathrm{in}}(0) = jA_R e^{-2jk_0 x_{RC}}$ and using the P-matrix in Eq. (2.8), we find $P_{11} = \phi^{-}_{\mathrm{out}}/\phi^{+}_{\mathrm{in}} = R$.

P_{11} is also expressed in COM theory in Eq. (2.23a). At center frequency ($\delta = 0$) and for small and constant $|\kappa|\lambda_0$, $P_{11} \approx -\kappa^*\lambda_0$ for a transducer with length of one unit cell (λ_0). Equating the two expressions for P_{11}, the reflection parameter per unit length can be expressed as

$$\kappa = -\frac{R^*}{\lambda_0} = j\frac{A_R}{\lambda_0}e^{2jk_0 x_{RC}}. \tag{2.29}$$

In conclusion, the three COM parameters (C_l, α and κ) for a FEUDT with six electrodes in one unit cell are determined using the quasi-static approximation and the COM analysis in Section 2.6.1. From the reflection parameter per unit length in Eq. (2.29), the transduction parameter per unit length in Eq. (2.27) and the capacitance per unit length in Eq. (2.26), the full P-matrix can be calculated and hence the S-matrix for a FEUDT.

The S-parameters for a FEUDT with 160 unit cells and 46 μm electrode overlap is shown in Figure 2.7. The maximum of S_{13} is -0.5 dB, but at this frequency the ratio of S_{13} and S_{23} (directivity) is only 10 dB while the maximum directivity is 30 dB. Close to the maximum of S_{13}, both S_{11} and S_{33} are low, while S_{22} is high. Reducing the acoustic reflection and maximizing the electric/SAW conversion in a transducer maximizes the performance of the resulting delay line. In this respect, the performance of the FEUDTs surpasses symmetric IDTs (Figure 2.3), for which S_{13} never exceeds -3 dB and the maximum of S_{13} coincides the maximum of S_{11}.

As can be seen in Figure 2.8 the COM model predicts that the directivity increases monotonically with number of unit cells. In order to achieve a directivity above 20 dB and impedance matching to 50 Ω, the FEUDTs require approximately 100 unit cells. In Chapter 4 we will see that this agrees well with our measurements. The directivity is independent of electrode overlap but impedance matching needs an electrode overlap larger than 25 μm.

†Here R does not include multiple transits.

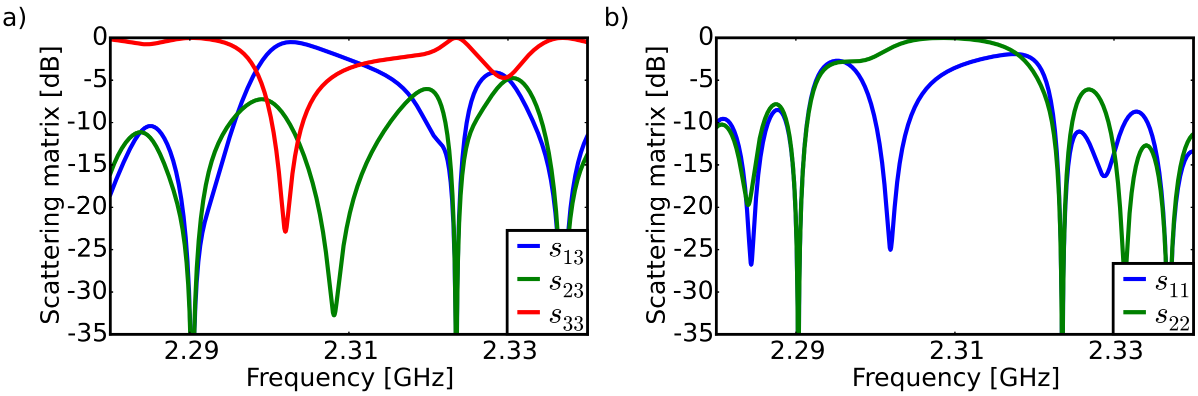

Figure 2.7: a) Scattering elements s_{13} (blue), s_{23} (green) and s_{33} (red) for a FEUDT with 160 unit cells and 46 μm electrode overlap. Both the electric reflection and the maximum directivity are offset the maximum transduction. b) Acoustic reflection scattering elements for both ports, where s_{22} (blue) is higher than s_{11} (green) and the dip in s_{11} coincides with the reflection dip in s_{33}.

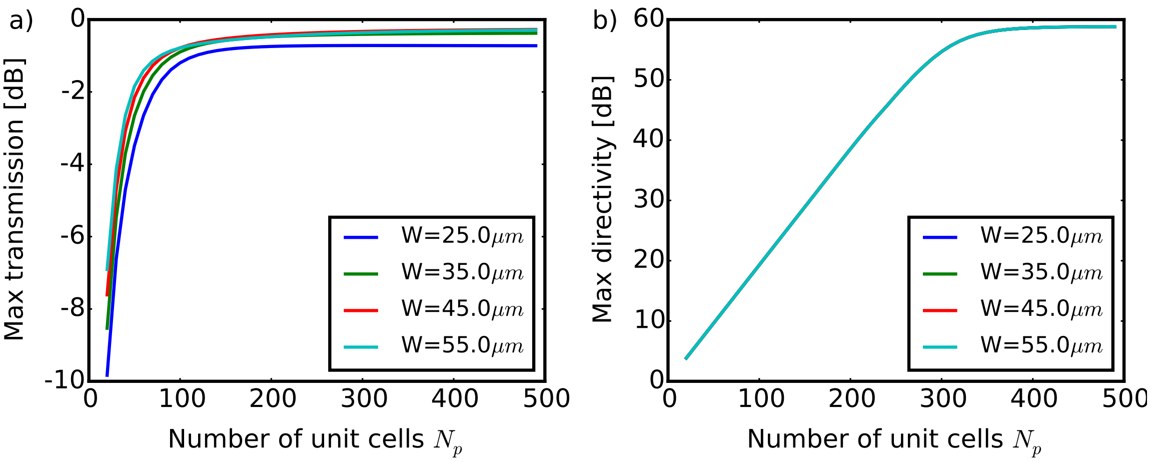

Figure 2.8: a) Maximum transmission versus number of unit cells N_p for a FEUDTs with different electrode overlaps W. At least 100 unit cells are needed to impedance match to 50 Ω. b) Maximum directivity versus N_p for FEUDTs. For a directivity above 20 dB, more than 100 unit cells are needed. The directivity does not depend on W.

Chapter 3

Experimental techniques

In order to perform the experiments, nanofabrication and precise measurements were done. The first section of this chapter describes the key processes used in the fabrication of the samples. The second section describes the measurement techniques, where the samples are cooled down to cryogenic temperatures in a dilution cryostat and measured at gigahertz frequencies.

3.1 Sample fabrication

All devices presented in this thesis were fabricated in the class 10-100 area of the MC2 Nanofabrication Laboratory at Chalmers University of Technology. They were SAW devices designed with two transducers separated on a piezoelectric substrate, either gallium arsenide (GaAs-(100)-[011]) or black linthium niobate ($LiNbO_3$-YZ). Regardless of the transducer types used, single or double electrode IDTs, FEUDTs or IDTs embedded in artificial atoms described in Chapter 2, they were made with 27 nm aluminum capped with 3 nm palladium connected to 85 nm think gold ground planes and electrodes. The gold pads had a sticking layer of 5 nm titanium and were capped with a 10 nm layer of palladium for better contact (resulting in a total pad thickness of 100 nm). The transducers in the qubits were in addition connected to aluminum SQUIDs, which were deposited in a separate fabrication step using two-angle evaporation and connected via the palladium layer on the transducers.

The fabrication techniques used are described briefly below, for more details the fabrication recipes can be found in Appendix A.

3.1.1 Photolithography for microscale features

In order to save processing time, photolithography was used to define features bigger than approximately 1 μm, which in our devices were contact pads, ground planes and alignment marks for later fabrication steps.

Prior to the photolithography, the cleaned substrate was coated with a bilayer of a lift-off resist and a positive photoresist. The two layers of resist had different properties and purposes; the top layer was used for patterning since it acquires sharp edges with high resolution, while the bottom layer improved the lift-off because it dissolves isotropically forming an undercut.

The photolithography was performed by first aligning the coated substrate carefully with a chromium pattered photomask and then exposing it to ultraviolet light through the photomask. The exposed coated substrate was immersed into a hydroxide solution for development. During the development, the exposed resist was dissolved while the resist that had been protected from the exposure by the photomask was left on the substrate. In this way, the negative pattern of the photomask was transferred onto the resist on the substrate.

After the development, the organic residues from the exposed resist were ashed away in an oxygen plasma. The desired metal was then deposited on the pattered substrate in an electron-beam evaporator with high vacuum. Finally, the remaining resist was dissolved in a solvent, which lifted-off the metal on top of the resist and left the patterned metal.

For a better flexibility of the pattern, contact pads and ground planes were in some cases written with a LASER writer instead of photolithography. In this process a LASER scans the resist-coated substrate in a similar way to the electron-beam which will be described in the following section.

3.1.2 Electron-beam lithography for micro- and nanoscale features

The smaller features of the devices, such as transducers and SQUIDs (Chapter 2.5), required higher resolution than possible with LASER and photolithography, necessitating the use of electron-beam lithography. In electron-beam lithography, a focused beam of electrons scans the substrate coated with electron-sensitive resist according to a programmable pattern. Since no mask is needed, the design is more flexible but the patterning is much slower. Otherwise, the electron-beam lithography steps are similar to the photolithography steps.

There are some difficulties associated with electron-beam lithography, including proximity and charging errors. Proximity effects limits the achievable resolution and are common when exposing narrow and dense patterns such as the transducers. The effect occurs when electrons scatter from the exposed areas to regions in the proximity and partially expose the unwanted areas. However, the proximity effect can be compensated for by calculating the dose profile for the substrate, divide the pattern into a mesh grid and distribute the doses according to the profile. This was done using the software BEAMER™.

Charging errors are minor on conducting or semi-insulating substrates such as gallium arsenide, but are usual on insulating substrates such as lithium niobate. On insulating substrates, electrons are not conducted away when the electron-beam scans the substrate. This leads to build up charge repelling electrons from the region, which can result in a small offset and a distorted pattern. Therefore, a thin conducting resist layer was used on top of the electron-sensitive resists on the lithium niobate substrates.

3.1.3 Two-angle evaporation for superconducting quantum interference devices

Some of the devices, with an artificial atom, went through additional fabrication steps where the transducer was connected to a SQUID. The SQUID was made using electron-beam lithography to create a suspended resist (Dolan) bridge and a technique called two-angle evaporation (shadow evaporation) [63].

This technique was used after the sample had been coated with resist, patterned by electron-beam lithography and developed. The sample was mounted onto a tilting stage in an electron-beam evaporator. First, the stage was tilted to a fixed angle at which the bottom aluminum layer was evaporated. Second, the aluminum covered substrate was exposed to pure oxygen gas at a regulated pressure for a certain amount of time, which formed a thin insulating barrier of amorphous aluminum oxide. Finally, after the oxygen was pumped out, the top aluminum electrode was deposited at the opposite angle. The metal was lifted-off, and the desired pattern was left on the substrate as described in the previous sections.

The thicknesses of the deposited aluminum were chosen such that the top layer overlapped the bottom layer with the insulating barrier in between. In addition, one aluminum layer contacted the grounded part of the transducer and the other layer contacted the live part (Figure 4.1b in Chapter 4.1) such that the SQUID was coupled in parallel with the transducer. This connection was possible using the thin palladium layer on top of the aluminum electrodes, which prevented the formation of aluminum oxide.

3.2 Cryogenic measurements

The aluminum transducers and SQUIDs were superconducting below approximately 1 K, but they were cooled down even further for the experiments. When conducting experiments at the quantum level, it is necessary to cool down to cryogenic temperatures and operate at microwave frequencies such that $k_B T \ll hf$. Therefore the sample in appended Paper I and II, which was measured at a base temperature of 20 mK in a wet dilution cryostat, was operated at frequency of 4.8 GHz. The transducer structure in appended Paper III was more complicated and needed more electrodes within one period, which reduced the size of the electrode width and made the fabrication a lot more problematic. The problem was somewhat reduced by operating at 2.3 GHz. For those measurements we used a dry dilution cryostat to cool down to 10 mK.

3.2.1 Cooling techniques

The cooling process in both the wet and the dry dilution cryostat takes place in a mixing chamber and is based on the phase separation occurring when a mixture of helium-3 (^{3}He) and helium-4 (^{4}He) is cooled down to temperatures below 0.8 K. The two phases have different concentrations of liquid ^{3}He, a ^{3}He rich phase (concentrated phase) and a

^{3}He poor phase (diluted phase). Since ^{3}He is lighter than ^{4}He, the concentrated phase accumulates on top of the diluted phase. When ^{3}He transits from the concentrated phase to the diluted phase across the phase boundary, heat is absorbed and this provides cooling of the mixing chamber.

As long as the concentration balance of ^{3}He in the two phases is in non-equilibrium, the ^{3}He transits from the concentrated phase to the dilute phase and provides cooling. This non-equilibrium is driven by pumping ^{3}He out of the dilute phase by distillation in the still, which is connected to the diluted phase in the mixing chamber. The still is heated and the ^{3}He evaporates from the still whereas very little ^{4}He is evaporated. This is due to the much larger vapor pressure of ^{3}He than ^{4}He at the still temperature (0.7 - 0.8 K).

The ^{3}He in the concentrated phase needs to be replaced continuously. This is done by pumping out the evaporated ^{3}He from the still and cooling it. At the still, a flow impedance ensures a high enough ^{3}He pressure for condensing. The cooling of the ^{3}He gas is done with different techniques in the wet and the dry dilution cryostat.

In the wet dilution cryostat, the dilution unit is isolated from a surrounding ^{4}He bath by an inner vacuum chamber (IVC). The surrounding ^{4}He bath is used to cool the ^{3}He before it is re-condensed in a closed volume in the 1 K-pot. The boiling point of ^{4}He is around 4 K at atmosphere and around 1.5 K when it is pumped, giving the 1 K-pot its name. The cooling power of the 1 K-pot is controlled by evaporative cooling of the ^{4}He bath funneled in from the ^{4}He bath. The flow into the 1 K-pot is adjusted by a needle valve and the evaporative cooling is achieved by pumping the ^{4}He.

In a dry dilution cryostat, the cooling of the ^{3}He gas is instead done with a pulse-tube cryocooler. It consists of several parts, three heat exchangers, a re-generator, a thermally isolated tube (pulse tube), a flow resistance and a buffer tank. A rotating valve oscillates the pressure at the warm side of the re-generator by connecting the system alternatingly to the high or low pressure side of a compressor. As a result, gas enters the system via the heat exchangers and moves inside the re-generator and pulse tube, before it is released again with a different temperature. When the gas moves inside the pulse tube, its temperature is changed by changing the pressure. One of the heat exchangers (connecting the re-generator to the pulse tube) is positioned at low temperature, where it absorbs heat and performs cooling.

After the liquid ^{3}He has been cooled by either one of the two techniques, the liquid ^{3}He is further cooled by heat exchangers at the different temperature stages, before it reaches the concentrated phase in the mixing chamber. A more detailed description on how a pulse tube cryocoler operates is described in Ref. [64].

3.2.2 Measurement set-up

Before the nanofabricated samples were cooled down, they were mounted and wire-bonded to a home-made sample box with SMA connectors. The sample boxes were attached to a magnetic coil, which was mounted at the mixing chamber stage. The mixing chamber stage was kept at a temperature of either 20 mK in the wet dilution cryostat or 10 mK in the dry dilution cryostat. The set-ups in both cryostats were very similar and a typical

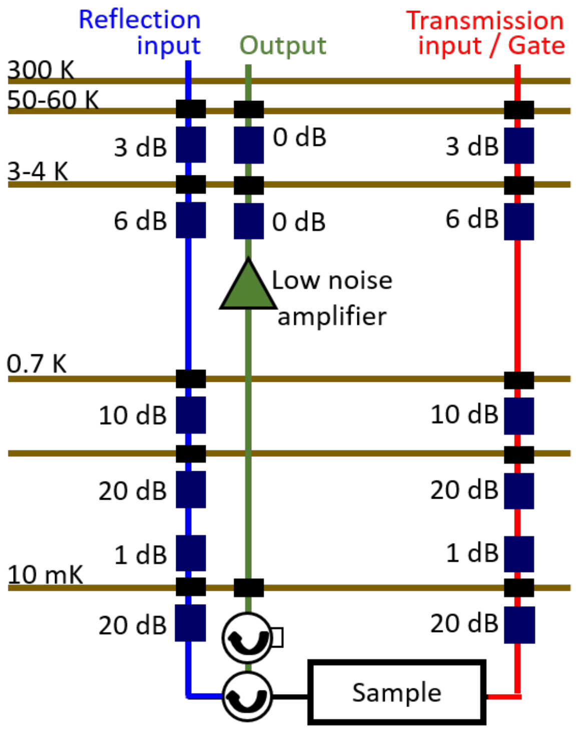

Figure 3.1: Measurement set-up enabling reflection and transmission measurements. Microwave signals were sent down an "reflection input" (blue) or a "transmission input/gate" (red) coaxial line, attenuated at every temperature stage before it reached the sample. The signal response of the sample passed two circulators (one working as an isolator) before it was amplified first with a low noise amplifier and then at room temperature via the "output" line (green).

set-up (for the dry dilution cryostat) is shown in Figure 3.1. In this set-up two types of measurements were possible; reflection (via blue and green lines) and transmission (via red and green lines).

The samples were measured via coaxial lines, which require careful design to not conduct black-body radiation from higher temperature stages to the samples. Therefore the coaxial lines have poor thermal conductivity and both the outer and inner conductors are thermalized at each temperature stage with an attenuator matching the noise temperature of that stage.

In the reflection measurements the microwave signal was sent via an "input" line (blue in Figure 3.1), reflected off the sample back to the same circulator, where the incoming and outgoing signals were separated. The outgoing signal went in the "output" line (green) passed another circulator before it was amplified with a low noise amplifier positioned at 4 K. This circulator was terminated with 50 Ω and worked as an isolator in order to absorb radiation noise coming down from the amplifier line. The amplified signal was further amplified at room temperature before it was measured.

In appended Paper I and II the "gate" line (red in Figure 3.1) was used to excited the qubit electrically. When the excited qubit relaxed, the emitted SAW propagated across the substrate and could be detected by the IDT. At the IDT it was converted back to electric signal, amplified and measured via the "output" line.

The "transmission input" line (red in Figure 3.1) was used for transmission measurements of the delay lines in appended Paper III. An electric signal sent via the transmission line to one of the transducers, where it was converted to SAWs. The SAWs propagated through the delay line and were detected by the other transducer, where they were converted back to electric signal, amplified and measured via the output line (green).

Chapter 4

Results

In this Chapter, the results of the appended papers are discussed. The interaction between SAWs and an artificial atom is demonstrated, motivating the need to improve the conversion between electric microwave signals and SAWs for future quantum SAW experiments. The improvement of the electric/SAW conversion using unidirectional transducers is also discussed.

4.1 Surface acoustic waves interacting with an artificial atom

An artificial atom coupling to SAWs was demonstrated for the first time in appended Paper I. The theory and fabrication for the experiment is described more in depth in appended Paper II, which is a book chapter that also covers theoretical and experimental work for SAW resonators at the quantum level. The SAW resonator work [21, 22] was done by the Leek Lab at the University of Oxford and will not be presented here.

The sample in appended Paper I and II (Figure 4.1) was measured at a base temperature of 20 mK. It has a single electrode IDT separated 100 μm apart from an artificial atom on the (100) surface of a polished gallium arsenide substrate with propagation along the [011] direction of the crystal. The pick up IDT has 125 unit cells of single electrodes, a center frequency of 4.8066 GHz and an emission bandwidth of about 1 MHz. The artificial atom is of the transmon type [54] described in Chapter 2.5. It uses a SQUID with a shunt capacitance made of a double electrode IDT structure with 20 unit cells, which enables the artificial atom to interact with SAWs. The top bus of the electrode structure is connected to one side of the SQUID and the bottom bus is connected to the other side and to ground (Figure 4.1b). The artificial atom has a maximum Josephson energy of 22.2 GHz, a charging energy and anharmonicity of 220 MHz and a bandwidth of 250 MHz. Its coupling to SAWs (acoustic coupling) $\Gamma_{\mathrm{ac}}/2\pi$ is 38 MHz, while its coupling to the electric gate is 0.75 MHz. The pure dephasing was estimated to be less than 10 % of the acoustic coupling. The acoustic coupling of the artificial atom is almost six times smaller than its anharmonicity, which made it possible to selectively address energy transitions both acoustically and electrically. Thus, it appeared as a qubit.

The qubit was measured in three ways using the set-up described in Chapter 3: via SAW reflection of the qubit using the IDT for emission and pick-up, via SAW detection with the IDT after electric excitation of the qubit through the gate and via two-tone spectroscopy. In the two-tone spectroscopy, the acoustic reflection was measured with

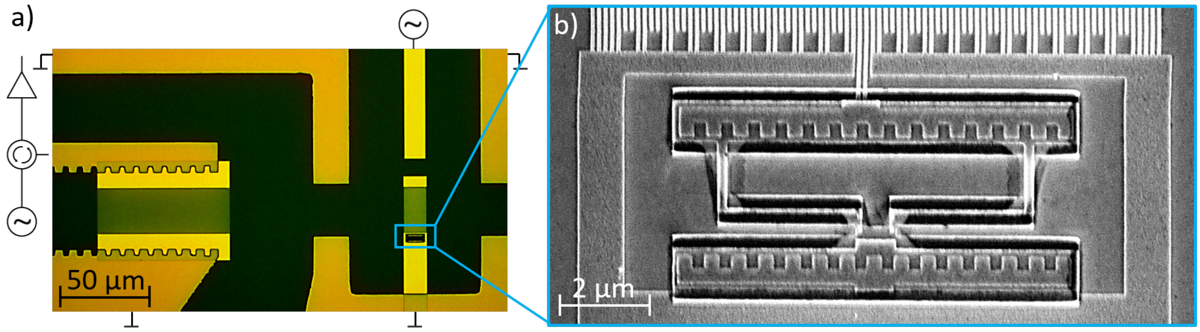

Figure 4.1: a) Optical micrograph of the sample discussed in appended Paper I and II. Electric signals were sent to or picked up by the single electrode IDT, shown to the left with its upper and lower bus in lighter yellow and its electrodes in blue. The IDT converted the signals into SAWs that propagated on the surface of the GaAs substrate (black) to the SAW artificial atom, shown to the right. The artificial atom could also be excited electrically with a gate, coming in from the top. b) Electron micrograph of the SQUID and its connection to the transducer, which formed the artificial atom coupled to SAWs.

the IDT while the qubit was irradiated with microwaves through the gate. Characterizing the qubit in those three ways, its non-classical nature and primary relaxation into SAWs could be demonstrated.

The non-classical nature of the qubit was highlighted by several different features. The first transition frequency of the qubit could be periodically tuned in and out of resonance with the IDT by changing the magnetic flux through the SQUID loop. This is shown in Figure 2b in appended Paper I and Figure 11 in appended Paper II. On resonance, the SAW beam emitted by the IDT was reflected back towards the IDT by the qubit. When the qubit was off resonance, the SAW beam passed the qubit without being reflected.

Furthermore, the reflected SAW power from the qubit was nonlinear in the excitation power (Figure 2f in appended Paper I). When the incoming power, $\mathrm{P}_{\mathrm{in}}/(hf) \ll \Gamma_{\mathrm{ac}}$, the qubit reflected the SAWs coming from the IDT. As the power increased the first excited state of the qubit became more populated and the reflection coefficient of the qubit decreased. At high powers, $\mathrm{P}_{\mathrm{in}}/(hf) \gg \Gamma_{\mathrm{ac}}$, the reflection coefficient tended to zero.

This behavior was also found when the qubit was excited through the gate and relaxed into SAWs, which were detected by IDT. The power dependence of the qubit transduction (blue dots) can be seen in Figure 4.2a, where the qubit transduction decreased nonlinearly with increasing power sent to the gate. At low powers, the power dependence of both the qubit reflection and transduction agreed with the semi-classical approximation (red line in Figure 4.2a) described Eq. (2.17) in Chapter 2.5. The semi-classical approximation also reproduced the reflected SAW power at higher powers, however at these powers the transduction deviated from the approximation. The deviation was captured by the full quantum model (green line in Figure 4.2) [32, 52] when six energy levels were included.

The SAW emission from the qubit was also detected while detuning the resonance frequency of the qubit by applying a magnetic flux though the SQUID loop. At low powers,

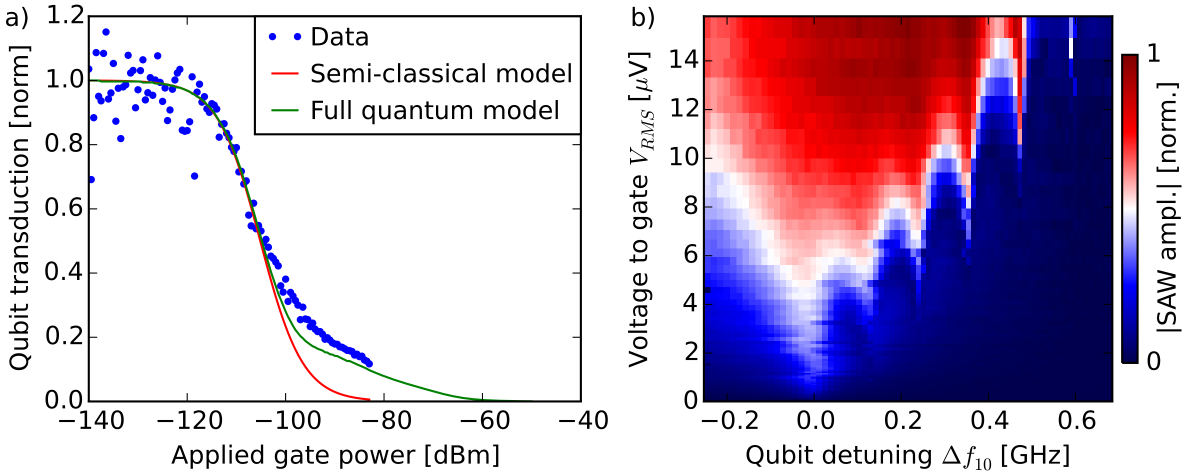

Figure 4.2: a) Qubit transduction from exciting it with the gate and detecting the emitted SAWs with the IDT versus applied power to the gate. The rate the qubit emits phonons is limited by Γ_{ac} and when the power to the gate $P_{\mathrm{gate}}/(hf) \gg \Gamma_{\mathrm{ac}}$ the transduction tends to zero. b) Transduction from the gate to the IDT versus applied power and qubit detuning. At higher power more than one photon from the gate could excited higher energy states at detuned frequencies. Here three higher levels are apparent.

the qubit could only be excited at its resonance frequency, but at higher powers several photons from the gate could together excite more energy states at detuned frequencies. This is shown in Figure 4.2b, where up to six transitions are visible. The transitions appear when the transition frequencies coincide with the driving frequency, and arise from the same type of physics as when the qubit was excited with SAWs from the IDT. The appearance of higher order energy transitions agree with the full quantum model, and this is shown in Figure 3 in appended Paper I for the first three energy transitions.

All of the above features show that the first energy transition could be addressed separately from transitions to higher energy states, meaning that the qubit could be treated as a two-level system. In addition, the acoustic coupling rate agreed with the semi-classical estimate in Eq. (2.16) in Chapter 2.5 (also in the supplementary material of appended Paper I and in appended Paper II). This highlights the non-classical nature of the qubit, together with two-tone spectroscopy further explored in appended Paper I. However, it is also important to demonstrate that the interaction is indeed acoustic. Therefore, measurements in the time domain were conducted.

Since the gate had a large bandwidth, it could be used to excite the qubit with both short (25 ns in Figure 12 in appended Paper II) and longer (1 μs in Figure 4 in appended Paper I) pulses at electric and acoustic resonance. An immediate electric crosstalk signal was measured at the IDT, due to capacitive coupling between the gate and the IDT. 40 ns later the SAW emitted by the qubit reached the IDT, which agreed well with the propagation distance and the SAW speed. The emitted SAW was not only picked up by the IDT, but also reflected back towards the qubit, where it was reflected again. This echo signal traveled three times the distance of the first SAW signal and was picked up by the IDT 80 ns later. For short pulses, three echoes spaced 80 ns apart could be observed. When longer pulses were used, the SAWs could either be in phase with the electric crosstalk or out of phase, which led to a 80 ns long stepwise increase or decrease of the measured signal. The measurements in the time domain prove that the qubit primarily relaxes by emitting SAW.

4.1.1 Loss estimation of the transducer

The data from the three types of measurements, were fitted using both the full quantm model [32, 52] summarized in appended Paper II and the semi-classical model in Chapter 2.5. These fits together with reflection measurement of the pick up IDT when the qubit was detuned (Figure 2a in Paper I), gave the scattering parameters in Table S1 in the supplementary material of appended Paper I. The electric reflection parameter $S_{33}{}^{\dagger}$ was estimated to 0.51 in amplitude units at the IDT center frequency, from direct measurements (using the same notation as in Chapter 2.2.1). This means that 26 % of the input signal was electrically reflected by the IDT.

For the remaining scattering parameters, we assume that the acoustic ports of the IDT are symmetric. Then a value of 0.28 and 0.55 in amplitude units were estimated for the electric/SAW conversion parameters $S_{13} = S_{23}$ and acoustic reflection parameters $S_{11} = S_{22}$, respectively. Accordingly, 8 % of the electric signal was converted into SAW in the desired direction and 30 % of the incoming SAW was acoustically reflected by the IDT.

If the power would be conserved the sum of the squared elements in each row of the scattering matrix in Eq. (2.7) in Chapter 2.2.1 is unity, which means that

$$S_{13}^2 + S_{23}^2 + S_{33}^2 = 1 \tag{4.1}$$

for the last row. The estimated values for S_{13} and S_{33} were used in Eq. (4.1) and the calculated sum was 0.42 in squared amplitude units, which means that 58 % of the power sent to the IDT was lost.

Both the high losses and the low bandwidth (1 MHz) are to some extent due to the substrate material. Gallium arsenide is a weak piezoelectric substrate, which has a low electric/SAW conversion and requires many unit cells to impedance match. The number of unit cells reduces the bandwidth of the IDT. The low electric/SAW conversion is obvious from the measurements, where only 8 % was converted in the desired direction. This is a problem when propagating SAWs are used for quantum experiments. To facilitate quantum SAW experiments, the electric/SAW conversion should be improved.

The conversion can be improved by changing the substrate to a stronger piezoelectric material, such as lithium niobate. This also reduces the number of unit cells needed for the impedance matching, and a double electrode IDT can be used with a higher bandwidth. However, all symmetric IDTs loose 50 % of the power theoretically, because the signal is converted into both acoustic ports and only one port aims into the device. Therefore, it is interesting to investigate transducers that are not emitting SAWs symmetrically.

†Different notation in appended Paper 1, where port 1 is the electric port, 2 is the acoustic port facing into the delay line and 3 is the other acoustic port *i.e.* $S_{11} = S_{33}$ here.

4.2 Improved conversion between electric signals and surface acoustic waves

In appended Paper I and II only 8 % of the SAWs was detected by the pick up transducer. In order to increase the electric/SAW conversion, we investigated both unidirectional transducers and IDTs on a stronger piezoelectric material in appended Paper III. The improved conversion efficiency by using a unidirectional transducer is the focus of this section.

All samples in appended Paper III are delay lines on black YZ lithium niobate ($LiNbO_3$), which has an about 70 times stronger electromechanical coupling coefficient than the gallium arsenide substrate in appended Paper I and II. The delay lines were measured at 2.3 GHz and 10 mK, and the results are summarized in Table 1 in appended Paper III. The delay lines consist of two transducers separated with an edge to edge distance L of 500 μm (Figure 4.3a). The transducers are either unidirectional transducers (UDTs) or double electrode interdigital transducers (IDTs). The UDTs have 110 (samples FEUDT_1-2) or 160 unit cells (samples FEUDT_3-4) in order to obtain optimized directivity and impedance match to 50 Ω, while the IDTs (Figure 4.3b) have 36 unit cells (samples IDT_1-3). Both transducer types have an electrode overlap of 35 or 46 μm.

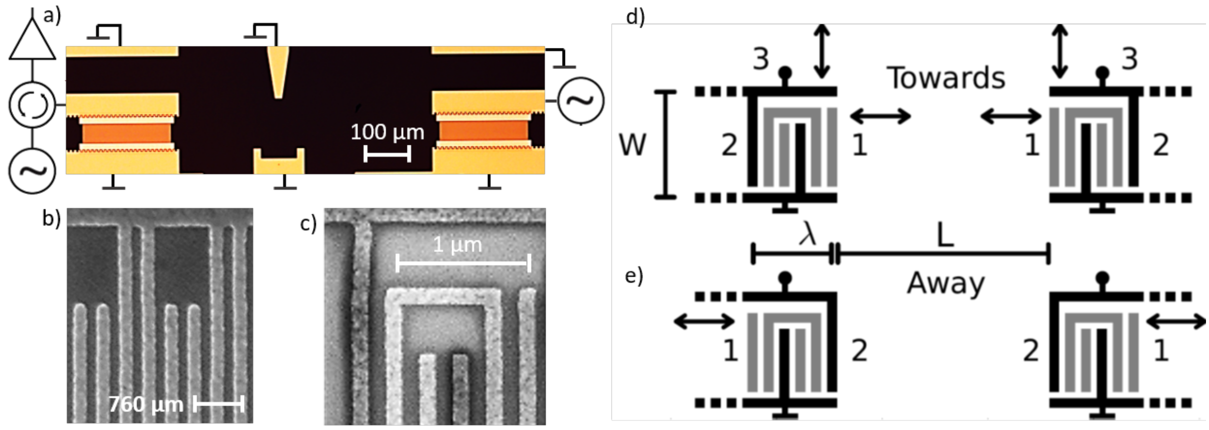

Figure 4.3: a) Optical micrograph of a delay line. Both transducers are either double electrode IDTs or FEUDTs. b) Electron micrograph of the top part of an IDT, where each unit cell has two electrodes connected to the live upper bus and two electrodes connected to the grounded bottom bus. c) Electron micrograph of the top part of one unit cell of a FEUDT. Note that the floating electrodes are brighter due to charging effects. The preferred electric/SAW conversion is towards the right [57], in port 1. d) A Towards delay line, where port 1 faces inwards and e) an Away delay line, where port 1 faces out from the device. One unit cell is illustrated, where the upper bus is connected to live electrodes, the lower bus is grounded and two of the floating electrodes (gray) are connected.

The UDT design, was selected from preliminary measurements of various types of UDTs at 860 MHz and room temperature [56]. It is based on a floating electrode unidirectional transducer (FEUDT) with six electrodes in one unit cell [57], seen in Figure 4.3c and described in Chapter 2.6.2. The design is such that electric/SAW conversion is optimized for port 1 and minimized for port 2 (Figure 4.3d). For optimal transmission, the FEUDTs were placed with port 1 facing into the delay line, *i.e.* port 1 of the two FEUDTs were towards each other. This type of delay line is described as "Towards". In order to compare the transmission through port 1 with port 2, we also measured "Away" delay lines (Figure 4.3e) where port 1 of the FEUDTs were facing out from the device.

The Fourier filtered transmission and reflection agreed well with the models (Figure 3 in appended Paper III), where the FEUDT delay lines were in excellent agreement with the COM theory in Chapter 2.6.1, and the IDT delay lines agreed well with the simple SAW circuit model described in Chapter 2.4.1. All Towards delay lines showed higher transmission than the IDT delay lines (Table 1 in appended Paper III). For instance, FEUDT_3-4 had on average 4.7 dB higher transmission than the IDT delay lines. Furthermore, all Towards delay lines exceeded the theoretical -6 dB minimum insertion loss limiting delay lines with standard symmetric IDTs. The transmission through the IDT delay lines was only -1.6±0.2 dB lower than the theoretical limit, which implies that their main source of loss is caused by their symmetric bi-directionality.

The directionality of the FEUDTs was measured by comparing the transmission through the Towards and the Away delay lines. A difference of 44 dB was observed (Table 1 in appended Paper III), which means a directivity of 22 dB per FEUDT and that 99.4 % of the power goes in the desired direction.

Part of the power was not converted back to electric signal, but was acoustically reflected back into the delay line by the transducer. These echo transits were Fourier filtered and fitted with the same model used for the main transmission and reflection, with the addition of the acoustic reflections as in Eq. (2.11) and (2.10) in Chapter 2.3. The agreement between the fits (dashed lines) and the first three transits (solid lines) in one FEUDT and one IDT delay line is shown in Figure 4.4a,b, where the first transit is the main transmission. After every transit less power was picked up, party because it was converted into electric power and partly because it was attenuated every time the SAW transited the delay line. Furthermore, the directivity of the FEUDT *i.e.* the ratio of the transited SAWs in the Towards and Away delay lines decreased for every transit (Figure 4.4c). This is due to the different acoustic reflection parameters for port 1 and port 2, explained in (Figure 2.7 in Chapter 2.6.1).

4.2.1 Loss estimation of delay lines

It total, -3.5±0.7 dB was lost during the main transmission in the Towards delay lines and -7.6±0.2 dB in the IDT delay lines, shown in Table 4.1. Most of this loss can be explained by the loss from conversion into the wrong acoustic port (directive loss) and propagation loss. The directive loss (γ_{D} in Table 4.1) is the dominating loss in the IDT delay lines and can account for -6 dB, but it can only account for -0.06 dB in the Towards delay lines.

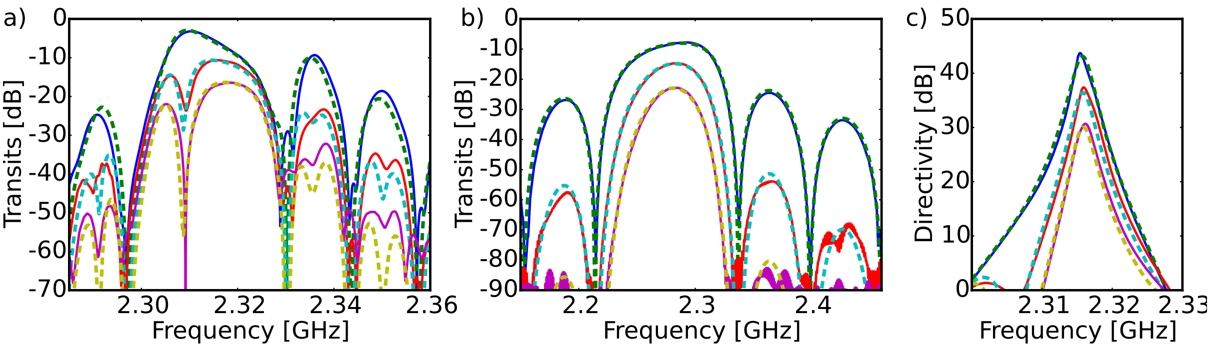

Figure 4.4: Multiple transits in a) sample FEUDT_3 Towards delay line fitted with the COM model and b) sample IDT_5 fitted with the SAW circuit model. The data is shown in solid lines and the fits as dashed lines. The main transmission is the highest in magnitude and each subsequent transit is smaller. All transits are fitted with the same center frequency, but with different attenuation. c) Directivity of sample FEUDT_2: the ratio between the SAW transits in the Towards and Away delay lines.

Table 4.1: The loss in maximum transmission (*Max T*) is higher than the total loss (γ_{tot}) due to directive loss (γ_{D}) and propagation loss. The propagation loss was estimated from loss due to viscous damping (γ_{vis}), beam steering (γ_{bs}) and diffraction (γ_{diff}) over the propagation distance $L + N_p\lambda$. γ_{ue} is the loss that cannot be explained by γ_{D} nor γ_{prop}.

Delay lines			$L + N_p\lambda$	*Max T*	Estimated loss [dB]					
Type	N_p	W[μm]	[μm]	[dB]	γ_{D}	γ_{vis}	γ_{bs}	γ_{diff}	γ_{tot}	γ_{ue}
FEUDT_1	110	35	665	-4.2	-0.06	-0.17	-0.37	-0.61	-1.2	-3.0
FEUDT_2	110	46	665	-3.7	-0.06	-0.17	-0.28	-0.77	-1.3	-2.4
FEUDT_3	160	46	740	-3.2	-0.06	-0.19	-0.31	-0.77	-1.3	-1.9
FEUDT_4	160	46	740	-2.8	-0.06	-0.19	-0.31	-0.77	-1.3	-1.5
IDT_1	36	35	554	-7.8	-6	-0.14	-0.31	-0.61	-7.1	-0.7
IDT_2	36	35	554	-7.7	-6	-0.14	-0.31	-0.61	-7.1	-0.6
IDT_3	36	46	554	-7.5	-6	-0.14	-0.23	-0.77	-7.1	-0.4

The propagation loss is expected to be similar in FEUDT and IDT delay lines, since all samples were fabricated simultaneously on the same wafer with a fixed transducer orientation and edge to edge transducer separation. However, the SAWs travel further underneath the transducers and the distance between the center of the transducer ($L + N_p\lambda$) is a better reference point. This distance is used to estimate the propagation loss (γ_{prop}), which may include beam steering, diffraction and viscous damping [44, 45].

The loss due to beam steering (γ_{bs} in Table 4.1) was estimated from the time the SAWs have to propagate in order to loose -3 dB [45],

$$B_{\text{-3dB}}[dB/s] = \frac{(1 - 1/\sqrt{2})W}{f\lambda_0 \tan(0.1|\delta\psi/\delta\theta|)}. \tag{4.2}$$

for an alignment error of 0.1° and frequency f. For our system, we get $B_{\text{-3dB}} \approx 2$ μs by using the slope of the power flow angle $|\delta\psi/\delta\theta| = -1.083$ for $LiNbO_3$ [44]. Assuming the

SAWs travel the distance $L + N_p\lambda$, the loss due to beam steering is estimated to about -0.3 dB.

The loss due to viscous damping was estimated from the attenuation coefficient, given by

$$\gamma_{\mathrm{att}}[dB/\mu s] = \gamma_{\mathrm{air}}(P)\frac{f}{10^9} + \gamma_{\mathrm{vis}}(T)\left(\frac{f}{10^9}\right)^2 \tag{4.3}$$

in air at room temperature [42]. The first term is due to air loading and the second is due to viscous damping in the substrate. Here, only the second term is important because the experiments were performed in vacuum and gas loading can be ignored. The calculated loss due to viscous damping was a bit more than -0.1 dB, using a viscous damping factor of 0.88 dB/(μsGHz^2) for $LiNbO_3$ at room temperature [45].

The diffraction loss (γ_{diff}) was linearly extrapolated from the results in Ref. [65]. It was estimated to around -0.7 dB, which indicates that it dominates the propagation loss.

The total estimation of the propagation loss is around -1.1 dB for all delay lines. Consequently, the propagation and directive loss cannot fully account for all loss in the delay lines, leaving an unexplained loss (γ_{ue} in Table 4.1) of -2.2±0.8 dB in the FEUDT Towards delay lines and -0.5±0.2 dB in the IDT delay lines. This loss is higher in the FEUDTs, probably because they have more unit cells. The loss per unit cell, -0.007±0.003 dB, is the same for both types of transducers.

The unexplained loss can be due to transducer imperfections and conversion into acoustic bulk waves. The loss due to transducer imperfections is much bigger at room temperature, when the resistance of the transducers is finite. In experiments with superconducting niobium FEUDTs at 3.5 K, the electrode resistance has been shown to have much bigger effect on the insertion loss than other loss mechanism [49]. Since our transducers were superconducting, this loss should be negligible.

Both the transducer imperfections and the conversion into bulk waves, affect the SAW every time it interacts with the transducer. In order to address the unexplained loss, we expand the three port scattering matrix in Eq. (2.7) in Chapter 2.2.1 to a four port scattering matrix

$$\begin{pmatrix} \phi^+_{out} \\ \phi^-_{out} \\ V^- \\ \phi_{\mathrm{Loss}} \end{pmatrix} = \begin{pmatrix} S_{11} S_{12} S_{13} S_{14} \\ S_{21} S_{22} S_{23} S_{24} \\ S_{31} S_{32} S_{33} S_{34} \\ S_{41} S_{42} S_{43} S_{44} \end{pmatrix} \begin{pmatrix} \phi^-_{in} \\ \phi^+_{in} \\ V^+ \\ 0 \end{pmatrix}, \tag{4.4}$$

where the fourth port describes the loss in the transducer, *i.e.* S_{41} is the loss during the acoustic reflection and S_{43} is the loss during the electric to SAW conversion. Both S_{43} and S_{41} contribute to the unexplained loss ($\gamma_{\mathrm{u.e.}}$). A schematic image over where the losses occur when two transducers are placed in a delay line is shown on Figure 4.5. The main transmission through the delay line suffers from electric reflection (S_{33}) before the electric signal is converted into SAWs. During the conversion, the power is lost to SAWs propagating in the undesired direction ($S_{32} = 2\gamma_{\mathrm{D}}$ from Table 4.1) and to conversion loss (S_{43}). The SAWs that propagate in the desired direction lose some power during the propagation (γ_{prop}) before they reach the other transducer. At the other transducer most of the power is converted to electric signal (S_{31}), but a part is acoustically reflected

(S_{11}), a small part is transmitted through the transducer (S_{21}) and some is lost (S_{41}). The acoustically reflected SAWs transit the delay line multiple times and every time γ_{prop} increases with the number of transits and S_{41} increases with the number of interactions with the transducers.

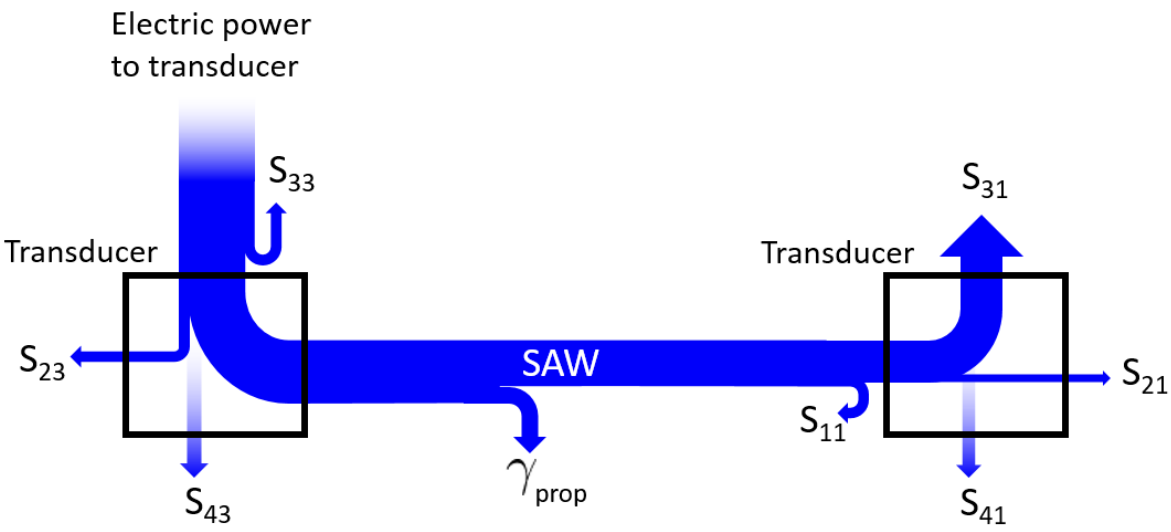

Figure 4.5: Illustration of loss in a delay line with two FEUDTs. For IDTs, S_{23} is of the same size as the signal through the delay line. When an electric signal is sent to a transducer, part of the signal is electrically reflected (S_{33}) and part of the signal is converted to SAWs both in the direction through the delay line, and in the undesired direction (S_{23}). A fraction of the signal is lost during the conversion (S_{43}). The SAW propagating through the delay line looses part of the power (γ_{prop}) before it reaches the other transducer. At the other transducer, the SAW is acoustically reflected (S_{11}), acoustically transmitted (S_{12}) and converted to electric signal (S_{31}). During this, part of the signal is lost (S_{41}). Both S_{43} and S_{41} contribute to the unexplained loss ($\gamma_{\text{u.e.}}$), while γ_{prop} can be theoretically estimated.

The loss during the main and multiple transits can be fitted (Figure 4.4) and the fitted attenuation increases for every transit. This increase is linear in dB, which can be seen in Figure 4.6 where it is fitted to the line

$$y(n_t) = (\gamma_{\text{prop}} + S_{41})n_t + S_{43} \tag{4.5}$$

for n_t number of transits. The y-intercept (S_{43}) implies the loss during the conversion from electric signals to SAWs. The slope of the lines ($\gamma_{\text{prop}} + S_{41}$) indicates the propagation loss during one transit (γ_{prop}) and the loss during one acoustic reflection (S_{41}). The propagation loss is the total estimated loss due to diffraction, beam steering and viscous damping. The scattering elements S_{33}, S_{23}, S_{31}, S_{11} and S_{21} does not contribute here, because they are already included in both the SAW circuit model and the COM model for fitting the transits. The result of the linear fits is shown in Table 4.2 for all delay lines.

The slope of $y(n_t)$ therefore gives $\gamma_{\text{prop}} + S_{41} \approx -0.9 \pm 0.1$ dB for all FEUDT delay lines, which is within the range of the estimated propagation loss. The similar value of around -1.3 dB for the IDT delay lines is also close to the estimated propagation loss, implying a very small or no loss during the acoustic reflection. The y-intercept gives

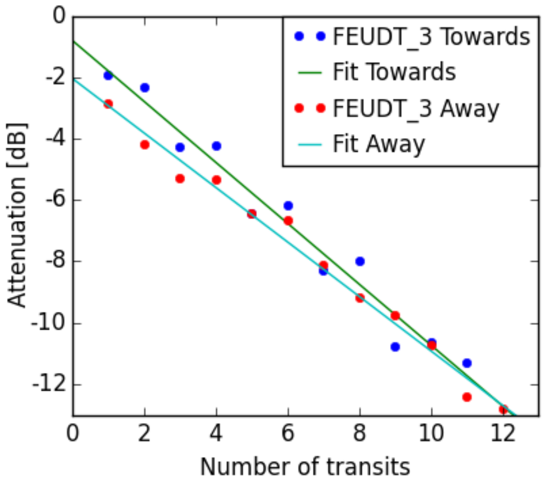

Figure 4.6: Attenuation of each transit in sample FEUDT_3 from COM fittings versus the number of times the SAW has transited the delay line. The attenuation of each delay line was linearly fitted on a logarithmic y-scale.

	Delay lines Type	Slope [dB]	y-intercept [dB]	$y(1)$ [dB]
Towards	FEUDT_1	-0.97	-1.3	-2.2
	FEUDT_2	-0.73	-1.9	-2.6
	FEUDT_3	-0.99	-0.81	-1.8
	FEUDT_4	-1.0	-1.2	-2.2
Away	FEUDT_1	-1.0	-2.3	-3.3
	FEUDT_2	-0.84	-2.2	-3.1
	FEUDT_3	-0.89	-2.0	-2.9
	IDT_1	-1.3	-0.59	-1.9
	IDT_2	-1.3	-0.36	-1.6
	IDT_3	-1.4	0.31	-1.1

Table 4.2: Result of linear fits to the attenuation versus transit. The slope describes $\gamma_{\text{prop}} + S_{41}$, while the y-intercept implies the loss S_{43}. The value of the linear fit at the first transit $y(1)$, estimates the loss for the main transmission.

$S_{43} \approx -1.5 \pm 0.7$ dB for FEUDT delay lines, whereas it is approximately -0.4 dB for IDT delay lines.

To sum up the losses, the biggest loss in the IDT delay lines is the directive loss, as theoretically predicted, and the remaining loss is mainly propagation loss. The directive loss is minimal in the Towards delay lines, and the transmission is high. Part of the loss in the transmission through the FEUDT delay line is lost during the propagation and this loss is dominated by diffraction loss, which can be improved with a bigger electrode overlap. However, the other part of the loss in the transmission through all types of delay lines cannot be attributed to propagation loss. This loss occurs every time the SAW interacts with the transducer, and scales with the number of unit cells with the same amount for both transducer types.

The estimated propagation loss on $LiNbO_3$ is comparable to similar estimations for GaAs, which was the substrate used in appended Paper I and II. For a 500 μm long delay line on GaAs the loss due to viscous damping would be around -0.2 dB, using Eq. (4.3) with a viscous damping factor of 0.9 dB/μs at room temperature [66]. Furthermore, the loss due to beam steering can be estimated to a bit less than -0.2 dB in the same way as for $LiNbO_3$ with a power flow angle of -0.537 for GaAs [45]. The diffraction could be estimated to -0.5 dB using a parabolic approximation [45]. In total, the propagation loss for the same type of delay lines on $LiNbO_3$ and on GaAs would be similar, but the loss during electric/SAW conversion is bigger on GaAs because it is a much weaker piezoelectric material.

4.2.2 Possibilities for quantum experiments

The electric/SAW conversion efficiency was improved by the use of the stronger piezoelectric substrate and by using FEUDTs in the Towards configuration instead of symmetric double electrode IDTs. Their 4.7 dB higher transmission than the IDT delay lines, is due to the 22 dB directivity of each FEUDT. However, the directivity was achieved with a certain number of unit cells, which results in a narrower bandwidth (Table 1 in appended Paper III). This is useful for on-chip filtering but can be a limitation in quantum SAW experiments.

In quantum SAW experiments, such as in appended Paper I and II, the qubit couples to SAW phonons using a transducer. This coupling is given by Eq. (2.16) in Chapter 2.5. Since the number of unit cells of the qubit transducer has to be at least one, the minimum acoustic coupling is approximately 100 MHz for a qubit on $LiNbO_3$ at 2.3 GHz. If the qubit coupling is bigger than the bandwidth of the pick up transducer, the qubit phonon emission will not activate all unit cells in the pick up transducer. Thus, there is a trade-off between bandwidth and directivity that needs to be optimized for a given experiment.

The minimum coupling of a qubit on $LiNbO_3$ is larger than the bandwidth of both the FEUDTs and the IDTs in appended Paper III, as it was for the SAW device in appended Paper I and II. In some quantum experiments it could be desirable to have a larger bandwidth of the pick up transducer than the qubit coupling and at the same time use the efficient electric/SAW conversion of the FEUDTs, then the qubit coupling needs to be decreased. This can be done by addressing the qubit transducer away from its center frequency on one of the side lobes [32, 52], by placing the qubit on a less piezoelectric substrate (appended Paper I and II) or by inserting an insulating layer between the qubit and the $LiNbO_3$ substrate [42].

Summary and outlook

In this thesis, we have studied propagating surface acoustic waves (SAWs) with the aim for quantum applications. In order to conduct experiments at the quantum level, the systems were cooled down to cryogenic temperatures and operated at microwave frequencies. The SAWs were generated and detected with periodic superconducting electrode structures forming an interdigital transducer (IDT). We demonstrated how such superconducting transducers can be unidirectional with high conversion efficiency and large directivity. We also showed how the SAWs can interact with an artificial atom at the quantum level. The devices were placed on a piezoelectric material, either gallium arsenide or lithium niobate.

In appended **Paper I**, we demonstrated the coupling between an artificial atom and SAWs for the first time. The first energy transition of the artificial atom could be addressed selectively and it could be tuned with magnetic flux. The acoustic reflection was measured and found to have a nonlinear power dependence. Transitions between more energy levels were detected at higher powers, and in addition, the relaxation of the artificial atom was proven to be dominantly into SAWs. These features highlights that the artificial atom coupled primarily to SAWs is of non-classical nature, which was suggested in Refs. [20, 67].

The theory, fabrication and future developments for the experiment was expanded on in appended **Paper II**, which is a chapter of the book *Superconducting Devices in Quantum Optics* [68]. Part of the theory summarizes a quantum model of the artificial atom coupling to a bosonic field at several separated points [32, 52]. The book chapter also includes theoretical and experimental work for SAW resonators at the quantum level, which is work done by the Leek Lab at the University of Oxford [21, 22].

The results in Paper I and II produce parallel findings from quantum optics but is perhaps best described as a different field, quantum acoustics. Quantum acoustics has a promising future to explore new regimes not easily feasible in its optical analogue. Many possible future developments were covered in appended Paper II, where the slow speed of the SAWs and the coupling strength between SAWs and artificial atoms are main contributors. One possibility of particular interest for this thesis, is how to detect and generate a single quantum of propagating sound (phonon). The detection of a single quantum of sound and other future quantum SAW experiments requires highly efficient electric/SAW conversion, which we have sought to address by reducing the primary source of loss in superconducting transducers.

An improved conversion between electric signals and SAWs was found in appended **Paper III**, where the SAW beam propagated between two floating electrode unidirectional transducers (FEUDTs) in a delay line geometry placed lithium niobate which is a strong piezoelectric material. The FEUDTs directed 99.4 % of power into the delay line, which means that only a few percent of power was lost in the undesired direction. This should be compared to the minimum theoretical loss of 50 % for a symmetric IDT. The improved conversion efficiency is useful for studying quantum physics with SAWs but there is a trade-off between bandwidth and directivity that needs to be optimized for a given experiment.

It should be possible to generate single phonons by exciting an artificial atom and letting it relax by emitting a SAW phonon in a Fock state. In order to prove the quantumness of the emitted sound, one would need to measure its second order correlation function. To do that, the bandwidth of the detecting transducer should be larger than the coupling of the artificial atom generating the phonon. The minimum coupling of an artificial atom on lithium niobate can be estimated to about 100 MHz and this is larger than the bandwidth of the FEUDTs. Either the coupling of the artificial atom needs to be decreased or the number of unit cells of the pick up transducer needs to be reduced at the cost of directivity and electric/SAW conversion. To keep the high electric/SAW conversion efficiency, the coupling of the artificial atom can be decreased by addressing its shunting transducer away from the center frequency at one of the side lobes of the response function [32, 52]. Alternatively, one could place the artificial atom on a less piezoelectric substrate (appended Paper I and II) or insert an insulating layer between the artificial atom and the piezoelectric substrate [42]. The reduction of coupling can be relaxed if the detecting transducers have less number of unit cells and instead the signal can be amplified with parametric amplifiers [69]. This combination could make a single SAW quantum distinguishable taking us towards measurements of quantum sound.

Appendix A

Cleanroom process

All samples were fabricated in the MC2 Nanofabrication Laboratory following the cleanroom process presented in this Chapter. The recipe includes the specific details for fabrication of delay lines and artificial atoms on $LiNbO_3$, but is similar for GaAs substrates. For GaAs the exposure time in the photolithography, the dose in the LASER writing and the electron-beam lithography and the development times are different, and the GaAs wafer was cleaved instead of diced.

1. Cleaning the wafer

1165 Remover	$60 - 70$°C, 10 min
Ultrasonic bath	100%, 1 min
IPA bath	Circulation 2 min
QDR bath	Rinse and blowdry with N_2

2. Photolithography to define alignment and chip marks

Stripping plasma	250 W, 40 sccm O_2, 10 min
Pre-bake in oven	170°C, 2 min
Spin lift-off resist LOR3B	6000 rpm, 1 min, $t_{acc} = 2$ s ($t \approx 300$ nm)
Softbake in oven	170°C, 10 min
Spin photoresist S1813	4000 rpm, 1 min, $t_{acc} = 2$ s ($t \approx 130$ nm)
Softbake on hotplate	110°C, 2 min
Expose pattern	MA6 mask aligner, Low-vac mode, $P_{vac} = 0.4$ bar 6 W/cm^2, $t_{exp} = 10$ s
Develop in MF319	90 s
QDR bath	Rinse and blowdry with N_2

3. Electron beam evaporation of metals in Lesker PVD225

Ashing in O_2-plasma	50 W, 10 s
E-beam evaporation	$P_{ch} \leq 10^{-7}$mbar Sticking layer (Ti), 5 nm , 10 nm/s Contact layer (Au), 85 nm, 10-20 nm/s Stopping layer (Pd), 10 nm, 10 nm/s
Lift-off in 1165 Remover	$60 - 70$°C, overnight
IPA bath	2 min
QDR bath	Rinse and blowdry with N_2

4. Dicing of wafer into quarters from backside

Pre-bake in oven	110°C, 2 min
Spin protective resist S1813	4000 rpm, 1 min, $t_{acc} = 2$ s ($t \approx 130$ nm)
Softbake on hotplate	110°C, 2 min
Align to photolithography marks	with backside alignment
Cuts through substrate (backside)	Dice the wafer into quartes
Strip resist in 1165 Remover	$60 - 70$°C, 10 min, sonicate 3 min
	Rinse in IPA and blowdry with N_2 ($\times$ 2 times)

5. Electron beam lithography for transducers

Ashing in O_2-plasma	50 W, 10 s
Pre-bake on hotplate	170°C, 3 min
Spin lift-off resist MMA/cop EL2	2000 rpm, $t_{acc} = 2$ s for 1 min
Softbake on hotplate	170°C, 5 min
Spin e-beam resist ZEP 520A(1:2)	3000 rpm, $t_{acc} = 2$ s, 1 min ($t \approx 300$ nm)
Softbake on hotplate	170°C, 5 min
Spinn E-spacer 300Z	2000 rpm $t_{acc} = 5$ s, 1 min
Softbake on hotplate	130°C, 2 min
Expose JEOL JBX-9300FS	100kV, 2nA,
	Nominal dose: 152 μC/cm^2 $LiNbO_3$,
	44 proximity corrected doses.
Remove E-spacer	QDR, blowdry with N_2
Develop top resist	N-Amyl-Acetate, 60 sec
	Blowdry with N_2
Develop bottom resist	MIKBK:IPA 1:1, 30 sec
	Blowdry with N_2

6. Electron beam evaporation of metals in Lesker PVD225

Ashing in O_2-plasma	50 W, 10 s
E-beam evaporation	$P_{ch} \leq 10^{-7}$mbar
	Contact layer (Al), 27 nm, 10 nm/s
	Stopping layer (Pd), 3 nm, 10 nm/s
Lift-off in 1165 Remover	$60 - 70$°C, overnight
IPA bath	2 min
H_2O bath	Rinse and blowdry with N_2

7. LASER writer for contact pads and ground planes

Stripping plasma	250 W, 40 sccm O_2, 1 min
Pre-bake on hotplate	170°C, 3 min
Spin protective resist MMA/cop EL2	2000 rpm, $t_{acc} = 2$ s for 1 min
Softbake on hotplate	170°C, 5 min
Spin lift-off resist LOR3A	6000 rpm, 1 min, $t_{acc} = 2$ s ($t \approx 250$ nm)
Softbake on hotplate	170°C, 5 min
Spin photoresist S1813	4000 rpm, 1 min, $t_{acc} = 2$ s ($t \approx 130$ nm)
Softbake on hotplate	110°C, 2 min
Expose	
Develop	MF319, 75 sec
	Rinse and blowdry with N_2
Remove copolymer	H_2O:IPA 1:4, 30 sec
	Rinse and blowdry with N_2
	Dip in new H_2O:IPA 1:4
	Rinse and blowdry with N_2

8. Electron beam evaporation of metals in Lesker PVD225

Ashing in O_2-plasma	50 W, 10 s
E-beam evaporation	$P_{ch} \leq 10^{-7}$mbar
	Sticking layer (Ti), 5 nm , 10 nm/s
	Contact layer (Au), 85 nm, 10-20 nm/s
	Stopping layer (Pd), 10 nm, 10 nm/s
Lift-off in 1165 Remover	$60 - 70$°C, overnight
IPA bath	2 min
	Rinse in IPA, water and blowdry with N_2

9. Electron beam lithography to define SQUIDs

Ozone	10 min
Pre-bake on hotplate	180°C, 3 min
Spin lift-off resist MMA EL10	2000 rpm, $t_{acc} = 2$ s for 1 min ($t \approx 570$ nm)
Softbake on hotplate	180°C, 5 min
Spin e-beam resist AR-P6200.13 1:2	2000 rpm, $t_{acc} = 2$ s, 1 min ($t \approx 100$ nm)
Softbake on hotplate	180°C, 5 min
Spinn E-spacer 300Z	2000 rpm $t_{acc} = 5$ s, 1 min
Softbake on hotplate	130°C, 2 min
Expose JEOL JBX-9300FS	100kV, 2nA,
	Nominal dose: 240 μC/cm^2 $LiNbO_3$,
	11 proximity corrected doses.
Remove E-spacer	QDR, blowdry with N_2

10a. Dicing of wafer from backside for devices with SQUIDs

Align to marks	with backside alignment
Cuts through substrate (backside)	Dice the quarters into chips

10b. Dicing of wafer from backside for devices without SQUIDs

Pre-bake in oven	110°C, 2 min
Spin protective resist S1813	4000 rpm, 1 min, $t_{acc} = 2$ s ($t \approx 130$ nm)
Softbake on hotplate	110°C, 2 min
Align to marks	with backside alignment
Cuts through substrate (backside)	Dice the quarters into chips
Strip resist in 1165 Remover	$60 - 70$°C, $t \approx 10$ min
	Rinse in IPA, water and blowdry with N_2 ($\times$ 2 times)

11. Two-angle evaporation of SQUIDs in Plassys

Develop top resist	n-amyl acetate, 90 s
Develop bottom resist	H_2O:IPA 1:4, 6 min
Ashing in oxygen plasma	50 W, 10 s
Electron beam evaporation	$P_{ch} \leq 2 \times 10^{-7}$ mbar
Bottom layer of Al	40 nm, 5Å/s, $\alpha = 15°$
Dynamic oxidation	$P_{ox} = 0,17$ mbar, $t_{ox} = 10$ min
Top layer of Al	60 nm, 5Å/s, $\alpha = -15°$
Lift-off in 1165 Remover	$60 - 70$°C, overnight
	Rinse in IPA, water and blowdry with N_2

Acknowledgments

I would like to start with expressing my gratitude towards my main supervisor professor Per Delsing for giving me the opportunity to carry out my doctoral studies in his group and for his confidence in my ability. I am also grateful for having professor Göran Johansson as my assistant supervisor. Both Per and Göran have an enthusiasm for physics and way of expressing science that motivates me to one day be able to do the same.

Next, I thank Thomas Aref who not only supervises me in the measurement laboratory but also takes the time to give me scientific feedback and support in writing. The work in this thesis would not have been possible without his scientific contribution, assistance and guidance.

This work was supported by The Swedish Research Council and The Knut and Alice Wallenberg foundation. The samples were made at the Nanofabrication Laboratory at Chalmers University of Technology.

I acknowledge former and present colleagues of the Quantum Device Physics Laboratory, the Applied Quantum Physics Laboratory and the Nanofabrication Laboratory, especially Martin Gustafsson for initiating this line of research, Sumedh Mahashabde for introducing me to nanotechnology, Henric Fjellstedt for recovering part of the work on my computer and Philip Krantz for the cover image and design of the appendix. I thank Anton Frisk Kockum as well as our bachelor students Johan Runeson, Johan Björck and Isac Boström. I am also thankful for the support from Tobias Wenger, Pier-Paolo Aurino, David Niepce, Susannah Carlsson, and Joel Lindkvist.

Finally, to my family and friends, thank you for allowing me to disappear into my work bubble and for your endless support.

Maria Ekström

Göteborg, November 2016

Bibliography

[1] J. D. Teufel, T. Donner, M. A. Castellanos-Beltran, J. W. Harlow, and K. W. Lehnert. Nanomechanical motion measured with an imprecision below that at the standard quantum limit. *Nat. Nanotech.*, 4:820, 2009.

[2] M. D. LaHaye, J. Suh, P. M. Echternach, K. C. Schwab, and M. L. Roukes. Nanomechanical measurements of a superconducting qubit. *Nature*, 459:960, 2009.

[3] A. D. OĆonnell, M. Hofheinz, M. Ansmann, R. C. Bialczak, M. Lenander, Erik Lucero, M. Neeley, D. Sank, H. Wang, M. Weides, J. Wenner, John M. Martinis, and A. N. Cleland. Quantum ground state and single-phonon control of a mechanical resonator. *Nature*, 464:697, 2010.

[4] J. M. Pirkkalainen, S. U. Cho, J. Li, G. S. Paraoanu, P. J. Hakonen, and M. A. Sillanpää. Hybrid circuit cavity quantum electrodynamics with a micromechanical resonator. *Nature*, 494:211, 2013.

[5] The Royal Swedish Academy of Sciences. The nobel prize in physics 2012 - advanced information, 2012. `www.nobelprize.org/nobel_prizes/physics/laureates/2012/advanced.html` (Visited 2016-11-11).

[6] D. J. Wineland. Nobel lecture: Superposition, entanglement, and raising schrödinger's cat. *Rev. Mod. Phys.*, 85:1103, 2013.

[7] S. Haroche. Nobel lecture: Controlling photons in a box and exploring the quantum to classical boundary. *Rev. Mod. Phys.*, 85:1083, 2013.

[8] C. Guerlin, J. Bernu, S. Deléglise, C. Sayrin, S. Gleyzes, S. Kuhr, M. Brune, J.-M. Raimond, and S. Haroche. Progressive field-state collapse and quantum non-demolition photon counting. *Nature*, 448:889, 2007.

[9] R Miller, T E Northup, K M Birnbaum, A Boca, A D Boozer, and H J Kimble. Trapped atoms in cavity qed: coupling quantized light and matter. *J. Phys. B.*, 38:S551, 2005.

[10] R. Hanson, L. P. Kouwenhoven, J. R. Petta, S. Tarucha, and L. M. K. Vandersypen. Spins in few-electron quantum dots. *Rev. Mod. Phys.*, 79:1217, 2007.

[11] M. V. G. Dutt, L. Childress, L. Jiang, E. Togan, J. Maze, F. Jelezko, A. S. Zibrov, P. R. Hemmer, and M. D. Lukin. Quantum register based on individual electronic and nuclear spin qubits in diamond. *Science*, 316:1312, 2007.

[12] H. de Riedmatten, M. Afzelius, M. U. Staudt, C. Simon, and N. Gisin. A solid-state light-matter interface at the single-photon level. *Nature*, 456:773, 2008.

[13] A. Wallraff, D. I. Schuster, A. Blais, L. Frunzio, R.-S. Huang, J. Majer, S. Kumar, S. M. Girvin, and R. J. Schoelkopf. Strong coupling of a single photon to a superconducting qubit using circuit quantum electrodynamics. *Nature*, 431:162, 2004.

[14] R. J. Schoelkopf and S. M. Girvin. Wiring up quantum systems. *Nature*, 451:664, 2008.

[15] H. Zheng, D. J. Gauthier, and H. U. Baranger. Waveguide qed: Many-body bound-state effects in coherent and fock-state scattering from a two-level system. *Phys. Rev. A*, 82:063816, 2010.

[16] H. Zheng, D. J. Gauthier, and H. U. Baranger. Waveguide-qed-based photonic quantum computation. *Phys. Rev. Lett.*, 111:090502, 2013.

[17] D. Valente, Y. Li, J. P. Poizat, J. M. Gérard, L. C. Kwek, M. F. Santos, and A. Auffèves. Optimal irreversible stimulated emission. *New J. Phys.*, 14:083029, 2012.

[18] I.-C. Hoi, C. M. Wilson, G. Johansson, J. Lindkvist, B. Peropadre, T. Palomaki, and P. Delsing. Microwave quantum optics with an artificial atom in one-dimensional open space. *New J. Phys.*, 15:025011, 2013.

[19] B.D. Josephson. Possible new effects in superconductive tunnelling. *Phys. Lett.*, 1:251–253, 1962.

[20] M. V. Gustafsson, P.V. Santos, G. Johansson, and P. Delsing. Local probing of propagating acoustic waves in a gigahertz echo chamber. *Nature Phys.*, 8:338, 2012.

[21] R. Manenti, M. J. Peterer, A. Nersisyan, E. B. Magnusson, A. Patterson, and P. J. Leek. Surface acoustic wave resonators in the quantum regime. *Phys. Rev. B*, 93:041411, 2016.

[22] E. B. Magnusson, B. H. Williams, R. Manenti, M.S. Nam, A. Nersisyan, M.J Peterer, A. Ardavan, and P. J. Leek. Surface acoustic wave devices on bulk zno at low temperature. *App. Phys. Lett.*, 106:063509, 2015.

[23] W. J. M. Naber, T. Fujisawa, H. W. Liu, and W. G. van der Wiel. Surface-acoustic-wave-induced transport in a double quantum dot. *Phys. Rev. Lett.*, 96:136807, 2006.

[24] C. H. W. Barnes, J. M. Shilton, and A. M. Robinson. Quantum computation using electrons trapped by surface acoustic waves. *Phys. Rev. B*, 62:8410–8419, 2000.

[25] S. Hermelin, S. Takada, M. Yamamoto, S. Tarucha, A. D. Wieck, L. Saminadayar, C. Bäuerle, and T. Meunier. Quantum physics: Single electrons take the bus. *Nature*, 477:435, 2011.

[26] R. P. G. McNeil, M. Kataoka, C. J. B. Ford, C. H. W. Barnes, D. Anderson, G. A. C. Jones, I. Farrer, and D. A. Ritchie. On-demand single-electron transfer between distant quantum dots. *Nature*, 477:439, 2011.

[27] E. A. Cerda-Méndez, D. N. Krizhanovskii, M. Wouters, R. Bradley, K. Biermann, K. Guda, R. Hey, P. V. Santos, D. Sarkar, and M. S. Skolnick. Polariton condensation in dynamic acoustic lattices. *Phys. Rev. Lett.*, 105:116402, 2010.

[28] V. S. Shumeiko. Quantum acousto-optic transducer for superconducting qubits. *Phys. Rev. A*, 93:023838, 2016.

[29] I. Buluta, S. Ashhab, and F. Nori. Natural and artificial atoms for quantum computation. *Rep. Prog. Phys.*, 74:104401, 2011.

[30] Y. Colombe, T. Steinmetz, G. Dubois, F. Linke, D. Hunger, and J. Reichel. Strong atom-field coupling for bose-einstein condensates in an optical cavity on a chip. *Nature*, 450:272, 2007.

[31] M. J. A. Schuetz, E. M. Kessler, G. Giedke, L. M. K. Vandersypen, M. D. Lukin, and J. I. Cirac. Universal quantum transducers based on surface acoustic waves. *Phys. Rev. X*, 5:031031, Sep 2015.

[32] A. Frisk Kockum, P. Delsing, and G. Johansson. Designing frequency-dependent relaxation rates and lamb shifts for a giant artificial atom. *Phys. Rev. A*, 90:013837, 2014.

[33] R. H. Hadfield. Single-photon detectors for optical quantum information applications. *Nat. Photon.*, 3:696, 2009.

[34] M. D. Eisaman, J. Fan, A. Migdall, and S. V. Polyakov. Invited review article: Single-photon sources and detectors. *Rev. Sci. Instrum.*, 82:071101, 2011.

[35] A. A. Houck, D. I. Schuster, J. M. Gambetta, J. A. Schreier, B. R. Johnson, J. M. Chow, L. Frunzio, J. Majer, M. H. Devoret, S. M. Girvin, and R. J. Schoelkopf. Generating single microwave photons in a circuit. *Nature*, 449:328, 2007.

[36] O. Astafiev, A. M. Zagoskin, A. A. Abdumalikov, Yu. A. Pashkin, T. Yamamoto, K. Inomata, Y. Nakamura, and J. S. Tsai. Resonance fluorescence of a single artificial atom. *Science*, 327:840, 2010.

[37] D. Bozyigit, C. Lang, L. Steffen, J. M. Fink, C. Eichler, M. Baur, R. Bianchetti, P. J. Leek, S. Filipp, M. P. da Silva, A. Blais, and A. Wallraff. Antibunching of microwave-frequency photons observed in correlation measurements using linear detectors. *Nature Phys.*, 7:154, 2011.

[38] C. Lang, D. Bozyigit, C. Eichler, L. Steffen, J. M. Fink, A. A. Abdumalikov, M. Baur, S. Filipp, M. P. da Silva, A. Blais, and A. Wallraff. Observation of resonant photon blockade at microwave frequencies using correlation function measurements. *Phys. Rev. Lett.*, 106:243601, 2011.

[39] I.-C. Hoi, T. Palomaki, J. Lindkvist, G. Johansson, P. Delsing, and C. M. Wilson. Generation of nonclassical microwave states using an artificial atom in 1d open space. *Phys. Rev. Lett.*, 108:263601, 2012.

[40] W. R. Smith, H. M. Gerard, J. H. Collins, T. M. Reeder, and H. J. Shaw. Design of surface wave delay lines with interdigital transducers. *IEEE Trans. Microwave Theory Tech.*, MTT-17:856, 1969.

[41] S. Datta. *Surface Acoustic Wave Devices*. Prentice-Hall, Englewood Cliffs, NJ, 1986.

[42] D. Morgan. *Surface Acoustic Wave Filters*. Academic Press, Amsterdam, second edition, 2007.

[43] C. Campbell. *Surface Acoustic Wave Devices and their Signal Processing Applications*. Academic Press, San Diego, 1989.

[44] A. J. Slobodnik Jr., P. H. Carr1, and A. J. Budreau. Microwave frequency acoustic surface-wave loss mechanisms on LiNbO3. *J. of Appl. Phys.*, 41:4380, 1970.

[45] A. J. Slobodnik Jr. *Materials and their influence on performance*, pages 225–303. Springer Berlin Heidelberg, Berlin, Heidelberg, 1978.

[46] J. H. Collins, H. M. Gerard, T. M. Reeder, and H. J. Shaw. Unidirectional surface wave transducer. *Proc. IEEE*, 57:833, 1969.

[47] K. Yamanouchi, C. H. S. Lee, K. Yamamoto, T. Meguro, and H. Odagawa. GHz-range low-loss wide band filters using new floating electrode type unidirectional transducers. *IEEE Ultrasonics Symp.*, 1:139, 1992.

[48] K. Yamanouchi, T. Meguro, Y. Wagatsuma, H. Odagawa, and K. Yamamoto. Nanometer electrode fabrication technology using anodic oxidation resist and application to unidirectional surface acoustic wave transducers. *J. of Appl. Phys.*, 33:3018, 1994.

[49] K. Yamanouchi. Generation, propagation and attenuation of 10 GHz-range SAW in LiNBO3. *IEEE Ultrasonics Symp.*, 1:57, 1998.

[50] L. Rayleigh. On waves propagated along the plane surface of an elastic solid. *Proceedings of the London Mathematical Society*, pages 4–11, 1885.

[51] R. M. White and F. W. Voltmer. Direct piezoelectric coupling to surface elastic waves. *Appl. Phys. Lett.*, 7:314, 1965.

[52] A. Frisk Kockum. *Quantum optics with artificial atoms*. PhD thesis, Chalmers University of Technology, 2014.

[53] T. W. Bristol, W. R. Jones, P. B. Snow, and W. R. Smith. Applications of double electrodes in acoustic surface wave device design. In *1972 Ultrasonics Symposium*, page 343. IEEE, 1972.

[54] J. Koch, T. M. Yu, J. Gambetta, A. A. Houck, D. I. Schuster, J. Majer, A. Blais, M. H. Devoret, S. M. Girvin, and R. J. Schoelkopf. Charge-insensitive qubit design derived from the cooper pair box. *Phys. Rev. A*, 76:042319, Oct 2007.

[55] B Peropadre, J Lindkvist, I-C Hoi, C M Wilson, J J Garcia-Ripoll, P Delsing, and G Johansson. Scattering of coherent states on a single artificial atom. *New J. Phys.*, 15(3):035009, 2013.

[56] I. Boström, J. Björck, and J. Runeson. Effektiv konvertering av ytakustiska vågor i en riktning. Bachelor's thesis, Chalmers University of Technology, Department of Microtechnology and Nanoscience, 2015.

[57] K. Yamanouchi and H. Furuyashiki. New low-loss SAW filter using internal floating electrode reflection types of single-phase unidirectional transducers. *Electron. Lett.*, 20:989, 1984.

[58] M. Takeuchi and K. Yamanouchi. Coupled mode analysis of SAW floating electrode unidirectional transducers. *IEEE Trans. UFFC*, 40:648, 1993.

[59] D. P. Morgan. Quasi-static analysis of floating-electrode unidirectional SAW transducers (feudts). *IEEE Ultrasonics Symp.*, 48:107, 1999.

[60] D. P. Morgan. Investigation of novel floating-electrode unidirectional SAW transducers. *IEEE Ultrasonics Symp.*, 1:15, 2000.

[61] D. P. Morgan. Quasi-static analysis of floating-electrode unidirectional SAW transducers. *IEEE Trans. UFFC*, page 15, 2001.

[62] M. Takeuchi and K. Yamanouchi. Field analysis of SAW single-phase unidirectional transducers using internal floating electrodes. *IEEE Ultrasonics Symp.*, 15:57, 1988.

[63] G. J. Dolan. Offset masks for lift-off photoprocessing. *Appl. Phys. Lett.*, 31:337, 1977.

[64] M. Simoen. *Parametric interactions with signals and the vacuum.* PhD thesis, Chalmers University of Technology, Department of Microtechnology and Nanoscience, 2015.

[65] T. Szabo and A. J. Slobodnik Jr. The effect of diffraction on the design of acoustic wave devices. *IEEE Trans. Sonics Ultrason.*, SU-20:240–251, 1973.

[66] W. D. Hunt, R. L. Miller, and B. J. Hunsinger. Slowness surface measurements for zero- and five-degree 100-cut GaAs. *J. Appl. Phys.*, 60:3532, 1986.

[67] Martin V. Gustafsson. *Studies of acoustic waves, noise and charge pumping using single-electron devices.* PhD thesis, Chalmers University of Technology, 2012.

[68] H. Robert Hadfield and Göran Johansson, editors. *Superconducting Devices in Quantum Optics.* Springer International Publishing, Cham, 2016.

[69] Philip Krantz. *The Josephson parametric oscillator - From microscopic studies to single-shot qubit readout.* PhD thesis, Chalmers University of Technology, 2016.